



Cite this: *Nanoscale*, 2016, **8**, 16357

Controlling the rectification properties of molecular junctions through molecule–electrode coupling†

Matthieu Koepf,‡§^a Christopher Koenigsmann,¶^{†a} Wendu Ding,||^a Arunbah Batra,^b Christian F. A. Negre,^c Latha Venkataraman,*^b Gary W. Brudvig,*^a Victor S. Batista,*^a Charles A. Schmuttenmaer*^a and Robert H. Crabtree*^a

The development of molecular components functioning as switches, rectifiers or amplifiers is a great challenge in molecular electronics. A desirable property of such components is functional robustness, meaning that the intrinsic functionality of components must be preserved regardless of the strategy used to integrate them into the final assemblies. Here, this issue is investigated for molecular diodes based on *N*-phenylbenzamide (NPBA) backbones. The transport properties of molecular junctions derived from NPBA are characterized while varying the nature of the functional groups interfacing the backbone and the gold electrodes required for break-junction measurements. Combining experimental and theoretical methods, it is shown that at low bias (<0.85 V) transport is determined by the same frontier molecular orbital originating from the NPBA core, regardless of the anchoring group employed. The magnitude of rectification, however, is strongly dependent on the strength of the electronic coupling at the gold–NPBA interface and on the spatial distribution of the local density of states of the dominant transport channel of the molecular junction.

Received 16th June 2016,
Accepted 16th August 2016
DOI: 10.1039/c6nr04830g

www.rsc.org/nanoscale

1. Introduction

The development of robust molecular components functioning as components of molecular integrated circuits is a primary goal of molecular electronics.^{1–4} Ultimately, nano-sized

components could permit the assembly of advanced sensors, logic gates, or energy conversion devices.⁵ An essential component for any such developments is the single molecule rectifier (or molecular diode).⁶

The implementation of molecular components into functional devices will require a detailed understanding of the fundamental relationship between the intrinsic performance of the component considered and the strategy used to interface it to the surrounding device architecture. Here, we investigate the influence of metallic contacts on the rectification properties of archetypal gold–diode–gold molecular junctions.

We focus on *N*-phenylbenzamide (NPBA) derivatives since earlier studies have indicated that they are good candidates for intrinsic rectification.⁷ Furthermore, they offer a stable molecular backbone of which the substitution pattern can be systematically tailored using robust synthetic strategies. Finally, their structural simplicity makes them accessible to advanced computational analysis and combinatorial methods for a detailed understanding of their electronic properties.^{7–9}

From an experimental perspective, the Scanning Tunneling Microscopy Break-Junction (STM-BJ)^{10,11} technique has enabled direct investigation of the transport properties of such derivatives.¹² In these measurements, the selected molecular backbone is interfaced with nanoscopic metallic electrodes (typically gold electrodes) *via* specific chemical functionalities that act as anchoring groups. In the case of simple molecular

^aDepartment of Chemistry & Energy Sciences Institute, Yale University, P.O. Box 208107, New Haven, Connecticut 06520-8107, USA. E-mail: gary.brudvig@yale.edu, victor.batisa@yale.edu, charles.schmuttenmaer@yale.edu, robert.crabtree@yale.edu

^bDepartment of Applied Physics and Applied Mathematics, Columbia University, Mail Code: 4701, New York, NY 10027, USA. E-mail: lv2117@columbia.edu

^cTheoretical Division, Los Alamos National Laboratory, Los Alamos, New Mexico 87545, USA

† Electronic supplementary information (ESI) available: Detailed synthetic procedures and full characterization of the derivatives; description of the leads used in the theoretical studies; details of the parameters used for the single state tight binding model; representation of the DOS of the three junctions; representation of the HOMO and LUMO state of an isolated NPBA backbone; determination of the angular dependence of the PDOS of the phenyl/anchor–lead fragments; and ¹H, ¹³C ¹⁹F NMR spectra of the derivatives. See DOI: 10.1039/c6nr04830g

‡ These authors contributed equally to this work.

§ Current address: Laboratoire de Chimie et Biologie des Métaux, CEA-CNRS-UGA UMR 5249, 17 avenue des martyrs 38054 Grenoble Cedex 9, France.

¶ Current address: Department of Chemistry, Fordham University, 441 East Fordham Road, Bronx, NY 10458, USA.

|| Current address: Department of Chemistry, Northwestern University, 2145 Sheridan Road, Evanston, IL 60208-3113, USA.



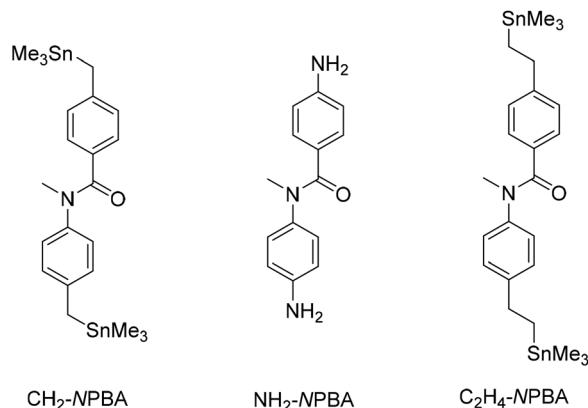


Fig. 1 Schematic drawing of the three NPBA derivatives investigated in this work.

wires, it has been shown that the nature of the anchoring groups can be of critical importance in determining the molecular states that govern the transport through the junction, and in controlling the strength of the electronic coupling between the backbone and the electrode materials.¹³

Rectification has been observed in molecular wires possessing symmetrical unsaturated backbones when different anchoring groups were employed on opposite termini of the wire, leading to a difference in the coupling to the gold leads.^{14,15} In molecular diode motifs with intrinsically asymmetric backbones, rectification is achieved even with symmetrical anchoring groups.^{16,17} Thus, a key question arises: how does coupling in symmetrically anchored metal-molecule-metal junctions influence the electronic properties and intrinsic rectification of molecular diodes such as NPBA derivatives? To address this question, we synthesized and analyzed a series of NPBA derivatives symmetrically substituted with a range of anchoring groups (Anchor-NPBA-Anchor, Anchor = CH_2 , NH_2 , or C_2H_4 , Fig. 1).

We studied the transport properties of the gold-NPBA-gold junctions by using a combined experimental and computational approach that allows for interpretation of STM-BJ measurements based on density functional theory (DFT) calculations, the non-equilibrium Green's function (NEGF) approach and a single-state tight-binding model based on the Breit-Wigner formula.¹⁸ Our findings demonstrate that within the range of bias considered (<0.85 V) the dominant transport channel of the junctions and the rectification mechanism remain the same throughout the series of NPBA derivatives, despite the changes in anchoring groups. However, for any given bias, the anchoring group significantly affects the experimentally determined conductance and magnitude of rectification.

2. Methods

STM break-junction measurements (STM-BJ)

The molecular conductance and current-voltage (I - V) characteristics were obtained utilizing a scanning tunneling micro-

scope (STM) in the break-junction mode.^{11,14} The break-junction technique relies on forming and breaking gold point contacts within a solution of the molecules of interest. A freshly cut gold wire (0.25 mm diameter, 99.999%, Alfa Aesar) and a mica disk coated with 100 nm of gold (99.999%, Alfa Aesar) were employed as the STM tip and substrate, respectively. The gold coated substrate was pre-treated in an UV-ozone etcher to remove residual organic impurities immediately before performing STM experiments. The STM break-junction measurements were performed under ambient, room temperature conditions. Initially, ~ 1000 conductance traces are collected with the pristine gold tip and substrate in order to verify that the tip and substrate are free of contaminants.

The conductance and I - V characteristics of the single molecule contacts are subsequently measured by forming junctions in the presence of a dilute solution of the desired molecule (1 mM–10 mM) dissolved in 1,2,4-trichlorobenzene (99%, Sigma Aldrich).¹⁹ The tip was brought into contact with the surface of the substrate until the conductance was greater than $5G_0$ ($1G_0 = 77.5 \mu\text{S}$). The tip was subsequently withdrawn at a rate of 15 nm s^{-1} for a period of 125 ms and held for a period of 150 ms, while a triangular voltage ramp was applied between +1 V and -1 V. Finally, the tip was withdrawn at 15 nm s^{-1} for a period of 75 ms to break the junction before repeating the process for a total of $\sim 50\,000$ individual traces. A data selection and sorting process, which is described in detail elsewhere,^{14,15} was then employed to generate the histograms of the I - V curves and determine the average I - V curve.

Computational methods

The isolated molecules were optimized at the DFT/B3LYP level using the 6-31++G(d,p) basis set as implemented in Gaussian 09 v.C01.²⁰ The molecular junctions were prepared by inserting the molecular backbones between two gold leads. The latter was modeled by using 6 layers of 16 gold atoms cut from a (111) fcc Au lattice. A gold triad was used to anchor the backbones as shown in Fig. S1.†⁷ The geometries of the junctions were optimized using the SIESTA computational package.²¹ During optimization the gold atoms forming the core of the leads were kept fixed in space (see the ESI†). The distance between the two leads was systematically varied to find the lowest energy geometry. The latter was used in the computations that followed. Zero-bias conductances were obtained by using the DFT-NEGF approach as implemented in Transiesta,²¹ with generalized gradient approximation (GGA) functional PBE²² and with the single- ζ basis set for gold atoms and the double- ζ basis set for the rest of the atoms.²¹ A Monkhorst-Pack k -point grid of $10 \times 10 \times 80$ was used to sample the Brillouin zone for the gold electrodes and a grid of $10 \times 10 \times 1$ for the molecular region. The energy cutoff for the real space grid was set to 200 Ry. Eigenchannels were computed using INELASTICA as implemented in the SIESTA computational package.²³ Rectification ratios were computed using a single-state tight-binding (TB) model, as described in detail elsewhere,²⁴ and in the ESI.†



3. Results and discussion

STM break-junction measurements (STM-BJ)

We synthesized the three derivatives $\text{CH}_2\text{-NPBA}$, $\text{NH}_2\text{-NPBA}$ and $\text{C}_2\text{H}_4\text{-NPBA}$, bearing methyl(trimethylstannyl), amino and ethyl(trimethylstannyl) substituents in the 4,4' positions, respectively (Fig. 1), to modulate the electronic properties of the interfaces between the gold electrodes and the conjugated NPBA backbone. The end-groups were selected to form covalent gold-carbon bonds following the surface-induced cleavage of the trimethylstannyl fragments,²⁵⁻²⁷ in the case of $\text{CH}_2\text{-NPBA}$ and $\text{C}_2\text{H}_4\text{-NPBA}$, or to form purely dative nitrogen-gold bonds^{28,29} in the case of $\text{NH}_2\text{-NPBA}$. With $\text{CH}_2\text{-NPBA}$ and $\text{NH}_2\text{-NPBA}$ derivatives, our specific aim was to probe the effect of the nature of the chemical bonding between the NPBA backbone and the electrodes on the properties of the respective junctions; $\text{C}_2\text{H}_4\text{-NPBA}$ was designed to investigate the consequences of minimizing the direct electronic coupling between the NPBA backbone and the anchoring points by adding a second methylene group on each end of the backbone.

All derivatives led to the formation of stable junctions in STM-BJ measurements and the current profiles under both fixed and variable bias were investigated. The distribution of conductances measured under fixed bias (≤ 0.025 V) for junctions derived from the three NPBA derivatives is presented in Fig. 2a. In each case, the average low-bias conductance (G) is determined from a fit of the conductance distribution of the corresponding junction. The G values obtained for the three different anchoring groups are shown in Table 1. The trend is consistent with prior results^{12,13} as well as with the theoretically calculated zero-bias conductances (G_{th}) (*vide infra*).

Table 1 Experimentally measured (G) and theoretically predicted (G_{th}) conductances; experimentally determined raw (RR), corrected (RR_c), and predicted (RR_{th}) rectification ratios for $\text{CH}_2\text{-NPBA}$, $\text{NH}_2\text{-NPBA}$, and $\text{C}_2\text{H}_4\text{-NPBA}$

Compound	G^a (G_0)	G_{th}^b (G_0)	RR ^c	RR _c ^d	RR _{th} ^e
$\text{CH}_2\text{-NPBA}$	1.0×10^{-3}	6.7×10^{-2}	2.0	1.8	1.8
$\text{NH}_2\text{-NPBA}$	9.4×10^{-5}	2.2×10^{-5}	1.6	1.4	1.2
$\text{C}_2\text{H}_4\text{-NPBA}$	8.5×10^{-6}	1.6×10^{-5}	1.4	1.2	1.1

^a Derived from the statistical analysis of STM-BJ traces measured at ≤ 0.025 V. ^b Determined from DFT-NEGF calculations at zero bias.

^c Derived from the analysis of STM-BJ traces measured under variable bias. The values are reported for 0.80 V. ^d Corrected for the contribution arising from the sorting process of the individual I - V curves (*cf.* text). ^e Calculated for an applied bias of 0.80 V.

The rectification ratio (RR) was determined from the asymmetry of the current-voltage (I - V) profile. Specifically, the RR is defined as the absolute value of the ratio of the current (I_+) measured in the positive voltage sweep with respect to the current (I_-) measured at the same voltage in the negative sweep: $\text{RR} = |I_+/I_-|$. For a fair comparison with the computed values (*vide infra*), at 0.8 V, the raw RR values can be corrected ($\text{RR}_c = \text{RR} - 0.2$) by removing the contribution that arises from the sorting process of the individual I - V curves, which produces a negligible RR of 1.2 in non-rectifying junctions based on *Z*-stillbene.¹⁴ Table 1 summarizes the measured RR and corrected RR_c, at 0.8 V, for the NPBA backbones with varying anchoring groups. In agreement with the previous reports,^{14,15} we observe an increase in the RR for all junctions upon increasing the applied bias up to 0.8 V (Fig. 2b).

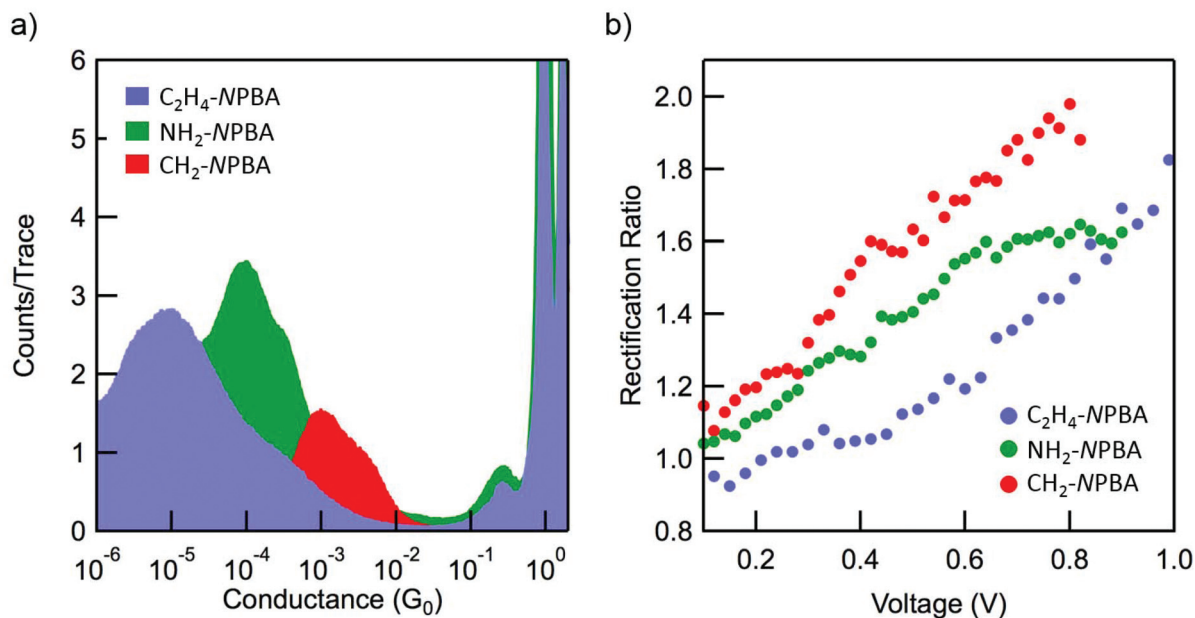


Fig. 2 (a) log-Binned conductance histograms for junctions formed with $\text{CH}_2\text{-NPBA}$, $\text{NH}_2\text{-NPBA}$ and $\text{C}_2\text{H}_4\text{-NPBA}$ between the gold electrodes. (b) Rectification ratio determined as a function of the bias for $\text{CH}_2\text{-NPBA}$, $\text{NH}_2\text{-NPBA}$ and $\text{C}_2\text{H}_4\text{-NPBA}$.



In the low bias regime (<0.85 V), the increase in the RR was found to correlate with the increase in conductance. The observation of a raw RR of ~ 2 at 0.8 V, for the junctions derived from $\text{CH}_2\text{-NPBA}$ is remarkable in the context of other STM-BJ measurements, especially considering the simplicity of the molecular structure investigated. To the best of our knowledge, it is one of the highest values reported thus far for this method at low bias, for intrinsic rectifiers. As minimal differences in the conformation of the NPBA cores are expected within this series, the large variations of conductance and rectification behavior observed among the junctions is most likely related to the modulation of the electronic coupling between the NPBA backbone and the metallic electrodes.

Computational analysis

The calculated and experimental values of zero-bias conductance (Table 1) followed the same trend though they differ in the actual magnitude due to the errors inherent to DFT.²⁹ In all the cases, a single transmission peak (closest to the Fermi level (E_F) of the junction) could be identified as the peak providing the dominant contribution to the transmission function (TF) (see Fig. 3a). By analyzing the local density of states (LDOS) for the three junctions, we identified the state that dominates transport, centered at $E_{\text{NPBA}} - E_F = -0.29$, -1.11 , and -1.58 eV for $\text{CH}_2\text{-NPBA}$, $\text{C}_2\text{H}_4\text{-NPBA}$, and $\text{NH}_2\text{-NPBA}$, respectively (see Fig. S2†).^{**} To support this assignment, the eigenchannels (projection of the eigenvectors of the transmission matrix on the atomic basis set) were computed at the energies mentioned above (see Fig. S3†).³⁰ We found that the symmetry of the eigenchannels is preserved throughout the series and is reminiscent of the symmetry of the isosurfaces of the LDOS calculated at E_{NPBA} (Fig. 3b–d and S3†). Thus, the latter states contribute significantly to the electron transport through the NPBA backbone. The representations of the isosurfaces of the LDOS at E_{NPBA} show strongly asymmetric distributions along the NPBA backbones, similarly for the three junctions (Fig. 3b–d). The distributions exhibit a clear homology with the LDOS calculated for the highest occupied molecular orbital (HOMO) of an isolated NPBA motif, where the density is mainly centered on the aminophenyl fragment (see Fig. S4†). These observations indicate that the electronic states (centered at E_{NPBA}) that dominate the transport share a common origin in the three junctions and are derived from the HOMO of the NPBA backbone. Previous studies have demonstrated that the low-bias rectification properties of NPBA derivatives are mainly determined by the asymmetric distribution of the electron density of the HOMO frontier orbital.^{7,8} Hence, the HOMO-derived electronic states likely control the transport properties of the junctions under both equilibrium and non-equilibrium regimes. From here on,

^{**} In the case of $\text{NH}_2\text{-NPBA}$, a peak centred at $+1.65$ eV is almost equally distant to E_F than compared to the dominant peak centred in the negative range (-1.58 eV). This suggests that both states might be controlling the transport properties of the junction. However, we will initially focus our analysis on the peak centred at -1.58 eV which nevertheless is the closest in energy to E_F .

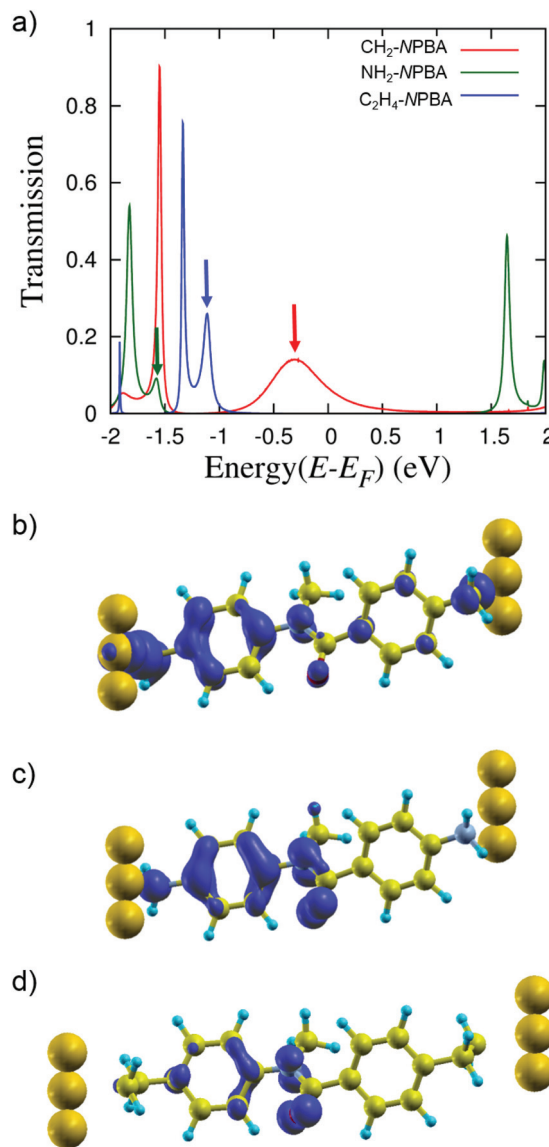


Fig. 3 (a) Overlay of the zero-bias transmission functions (TF) computed for the junctions formed with $\text{CH}_2\text{-NPBA}$ (red line), $\text{NH}_2\text{-NPBA}$ (green line), and $\text{C}_2\text{H}_4\text{-NPBA}$ (blue line) derivatives. In each TF the peak closest to the Fermi level (E_F), which dominates the transport properties of the junctions under low bias, is indicated with an arrow. (b), (c) and (d) Representations of the isosurfaces of the local density of state (LDOS) at the energy E_{NPBA} of the electronic state identified as the major contributor to the TF for the junction formed with $\text{CH}_2\text{-NPBA}$ (b), $\text{NH}_2\text{-NPBA}$ (c) and $\text{C}_2\text{H}_4\text{-NPBA}$ (d).

these states are referred to as the dominant transport channels.

To determine the RR under non-equilibrium conditions, we employed a single state tight-binding (TB) model based on the Breit–Wigner formula and computed I - V curves for the different Au–NPBA–Au junctions (see the ESI† for details). The model, parameterized from the zero-bias transmission function (Table S1†), simulates the energy shift of the dominant transport channel (E_{NPBA}), according to the applied bias, and



provides an approximation of the transport properties of the junctions under non-equilibrium conditions. The TB model provides remarkably good agreement between the RR_{th} and RR_c values (Table 1). These results confirm the critical role of the dominant transport channels identified above in the transport properties of all three junctions.

The nature of the anchoring groups significantly affects the energy alignment and broadening of the TF peaks shown in Fig. 3a, although the dominant transport channel for the three junctions is similar. Thus, the anchoring groups within this series primarily modulate the electronic coupling strength between the gold contacts and the NPBA HOMO. The coupling at the interface (as determined from the TB model) increases as follows: $NH_2 < C_2H_4 \ll CH_2$, while the trend observed for both G and RR is: $C_2H_4 < NH_2 \ll CH_2$. The inversion of the order for C_2H_4 - and NH_2 -NPBA can be rationalized in terms of the efficiency of the coupling between gold and the specific subsets of molecular orbitals that dominate transport (here the π -based HOMO of the NPBA backbone; *vide infra*).

First, we focused on the junctions formed by CH_2 - and NH_2 -NPBA, which share the closest structural similarity in the set. For these junctions, we observe a strong difference in the ability of the gold leads to couple into the π -system of the NPBA core, despite the formation of formal σ bonds in each case (either dative $N \rightarrow Au$ or covalent $C-Au$ bonds). To understand this difference, we examined the ratio of the projected density of states (PDOS) of the phenyl fragment ($PDOS_{Ph}$) to the adjacent Au-anchor motif ($PDOS_{Au-Anchor}$). Specifically, we investigated the variation of the ratio $PDOS_{Ph}/PDOS_{Au-Anchor}$ as the phenyl group is rotated about the axis defined by the anchor-phenyl bond (see Fig. S6 and S7†). In this analysis, a large angle-dependent variation of the ratio $PDOS_{Ph}/PDOS_{Au-Anchor}$ indicates that there is a significant redistribution of the electronic density as the Au-Anchor and phenyl units are rotated with respect to each other from the equilibrium geometry. Such a redistribution can in turn be interpreted as the modulation of the electronic coupling between the Au-Anchor motif and the phenyl π -system, where the more coupled system exhibits the most homogeneously distributed density (*e.g.* PDOS ratio closest to 1).

In the case of CH_2 -NPBA, we observe a significant angle dependence of $PDOS_{Au-Anchor}/PDOS_{Ph}$, with a 7-fold increase of the ratio as the angle varies from $+0$ to $+90^\circ$ relative to the equilibrium geometry (*cf.* Table S2†). Since a direct π - π overlap is excluded due to the pure sp^3 hybridization of the benzylic carbon, this observation suggests that the strong electronic coupling can be attributed to the hyperconjugation between the quasi-covalent $C-Au$ σ bond and the π -system of the NPBA.³¹ The electronic interaction between the benzylic $C-Au$ bond and the aromatic π -system, initially postulated^{14,26} and recently demonstrated experimentally²⁵ for (oligo)phenylenes, is thus well captured by our DFT analysis. On the other hand, the NH_2 -NPBA-based junction exhibits a much smaller angle dependence of $PDOS_{Au-Anchor}/PDOS_{Ph}$ with a 2-fold variation of this ratio as the angle is rotated from $+0$ to $+90^\circ$ from the equilibrium geometry. This is expected since the $N \rightarrow Au$ dative

bond in NH_2 -NPBA is significantly more polarized than the $C-Au$ bond, which reduces the strength of interactions through hyperconjugation.

In the case of C_2H_4 -NPBA, a strong hybridization between the gold leads and the terminal carbons of the backbone accounts for the larger electronic coupling compared to NH_2 -NPBA. However, the π -system of the former remains isolated from the Au-C interface due to the additional methylene group on either side of the backbone. In this case, hyperconjugation cannot occur and the spatial distribution of the local density of states of the dominant transport channel remains strongly localized towards the center of the junction. It results in poorly conductive and virtually non-rectifying junctions in the STM-BJ measurements at low bias.

4. Conclusion

Our results highlight the intimate relationship between the chemical nature of the anchoring groups and the observed electronic properties (conductance and rectification) of molecular junctions built from the NPBA molecular diode, in the case of a symmetrically anchored system. This complements earlier reports on the rectification properties of the junctions featuring asymmetrically coupled molecular wires.^{14,15,32} In particular, we demonstrate that the RR of a molecular backbone with intrinsic rectification can be enhanced by a suitable choice of the anchors, which in our case reaches a remarkable RR of ~ 2 as observed in STM-BJ measurements at low bias (< 0.85 V). Importantly, we show that variation of the anchoring groups does not fundamentally affect the nature of the dominant transport channel of the NPBA-based junctions; however, it affects the coupling into the asymmetrically localized molecular state (HOMO of the NPBA backbone) directly responsible for rectification. An important hypothesis stemming from our analysis is that hyperconjugation can play a critical role in allowing for efficient electronic coupling between the gold states and the HOMO level of the NPBA backbone, while preserving the essential characteristics of the latter (asymmetrically distributed along the junctions). It is, therefore, natural to conjecture that hyperconjugation, rarely considered in the design of molecular components, may provide an efficient approach to integrate individual molecules into advanced functional assemblies, without compromising the intrinsic properties of the constituent components.

Acknowledgements

We thank the Yale West Campus Analytical Core staff for help with instrumentation. This work was funded by the U.S. Department of Energy Grant DE-FG02-07ER15909 and a generous gift from the TomKat Charitable Trust. V. S. B. acknowledges NERSC support as part of the Argonne-Northwestern Solar Energy Research (ANSER) Center, an Energy Frontier Research Center funded by the U.S.



Department of Energy, Office of Science, Office of Basic Energy Sciences under award no. DE-SC0001059. L. V. thanks the Packard Foundation for support. A. B. was supported by the NSF GRFP Grant No. DGE-07-07425.

Notes and references

- 1 M. Ratner, *Nat. Nanotechnol.*, 2013, **8**, 378–381.
- 2 C. Joachim, J. K. Gimzewski and A. Aviram, *Nature*, 2000, **408**, 541–548.
- 3 J. R. Heath, *Annu. Rev. Mater. Res.*, 2009, **39**, 1–23.
- 4 R. M. Metzger, *Chem. Rev.*, 2015, **115**, 5056–5115.
- 5 S. J. van der Molen, R. Naaman, E. Scheer, J. B. Neaton, A. Nitzan, D. Natelson, N. J. Tao, H. van der Zant, M. Mayor, M. Ruben, M. Reed and M. Calame, *Nat. Nanotechnol.*, 2013, **8**, 385–389.
- 6 W. Ding, C. F. A. Negre, J. L. Palma, A. C. Durrell, L. J. Allen, K. J. Young, R. L. Milot, C. A. Schmittenmaer, G. W. Brudvig, R. H. Crabtree and V. S. Batista, *ChemPhysChem*, 2014, **15**, 1138–1147.
- 7 W. Ding, C. F. A. Negre, L. Vogt and V. S. Batista, *J. Chem. Theory Comput.*, 2014, **10**, 3393–3400.
- 8 W. Ding, M. Koepf, C. Koenigsmann, A. Batra, L. Venkataraman, C. F. A. Negre, G. W. Brudvig, R. H. Crabtree, C. A. Schmittenmaer and V. S. Batista, *J. Chem. Theory Comput.*, 2015, **11**, 5888–5896.
- 9 A. Monti, C. F. A. Negre, V. S. Batista, L. G. C. Rego, H. J. M. de Groot and F. Buda, *J. Phys. Chem. Lett.*, 2015, **6**, 2393–2398.
- 10 B. Q. Xu and N. J. J. Tao, *Science*, 2003, **301**, 1221–1223.
- 11 M. Kamenetska, M. Koentopp, A. C. Whalley, Y. S. Park, M. L. Steigerwald, C. Nuckolls, M. S. Hybertsen and L. Venkataraman, *Phys. Rev. Lett.*, 2009, **102**, 126803.
- 12 F. Schwarz and E. Loertscher, *J. Phys.: Condens. Matter*, 2014, **26**, 74201–74201.
- 13 V. Kaliginedi, A. V. Rudnev, P. Moreno-Garcia, M. Baghernejad, C. Huang, W. Hong and T. Wandlowski, *Phys. Chem. Chem. Phys.*, 2014, **16**, 23529–23539.
- 14 A. Batra, P. Darancet, Q. Chen, J. S. Meisner, J. R. Widawsky, J. B. Neaton, C. Nuckolls and L. Venkataraman, *Nano Lett.*, 2013, **13**, 6233–6237.
- 15 A. Batra, J. S. Meisner, P. Darancet, Q. Chen, M. L. Steigerwald, C. Nuckolls and L. Venkataraman, *Faraday Discuss.*, 2014, **174**, 79–89.
- 16 M. Elbing, R. Ochs, M. Koentopp, M. Fischer, C. von Hänisch, F. Weigend, F. Evers, H. B. Weber and M. Mayor, *Proc. Natl. Acad. Sci. U. S. A.*, 2005, **102**, 8815–8820.
- 17 I. Diez-Perez, J. Hihath, Y. Lee, L. Yu, L. Adamska, M. A. Kozhushner, I. I. Oleynik and N. Tao, *Nat. Chem.*, 2009, **1**, 635–641.
- 18 J. C. Cuevas and E. Scheer, *Molecular Electronics: An Introduction to Theory and Experiment*, World Scientific Publishing Company Pte Limited, 2010.
- 19 J. R. Widawsky, M. Kamenetska, J. Klare, C. Nuckolls, M. L. Steigerwald, M. S. Hybertsen and L. Venkataraman, *Nanotechnology*, 2009, **20**, 434009.
- 20 M. J. Frisch, G. W. Trucks, H. B. Schlegel, G. E. Scuseria, M. A. Robb, J. R. Cheeseman, G. Scalmani, V. Barone, B. Mennucci, G. A. Petersson, H. Nakatsuji, M. Caricato, X. Li, H. P. Hratchian, A. F. Izmaylov, J. Bloino, G. Zheng, J. L. Sonnenberg, M. Hada, M. Ehara, K. Toyota, R. Fukuda, J. Hasegawa, M. Ishida, T. Nakajima, Y. Honda, O. Kitao, H. Nakai, T. Vreven, J. A. Montgomery Jr., J. E. Peralta, F. Ogliaro, M. Bearpark, J. J. Heyd, E. Brothers, K. N. Kudin, V. N. Staroverov, R. Kobayashi, J. Normand, K. Raghavachari, A. Rendell, J. C. Burant, S. S. Iyengar, J. Tomasi, M. Cossi, N. Rega, J. M. Millam, M. Klene, J. E. Knox, J. B. Cross, V. Bakken, C. Adamo, J. Jaramillo, R. Gomperts, R. E. Stratmann, O. Yazyev, A. J. Austin, R. Cammi, C. Pomelli, J. W. Ochterski, R. L. Martin, K. Morokuma, V. G. Zakrzewski, G. A. Voth, P. Salvador, J. J. Dannenberg, S. Dapprich, A. D. Daniels, Ö. Farkas, J. B. Foresman, J. V. Ortiz, J. Cioslowski and D. J. Fox, *Vol. Revision A.1*, Gaussian, Inc., Wallingford, CT, 2009.
- 21 M. Brandbyge, J.-L. Mozos, P. Ordejón, J. Taylor and K. Stokbro, *Phys. Rev. B: Condens. Matter*, 2002, **65**, 165401.
- 22 J. P. Perdew, K. Burke and M. Ernzerhof, *Phys. Rev. Lett.*, 1996, **77**, 3865–3868.
- 23 <https://sourceforge.net/p/inelastica/code/HEAD/tree/>.
- 24 C. Koenigsmann, W. Ding, M. Koepf, A. Batra, L. Venkataraman, C. F. A. Negre, G. W. Brudvig, R. H. Crabtree, V. S. Batista and C. A. Schmittenmaer, *New J. Chem.*, 2016, DOI: 10.1039/C6NJ00870D, in press.
- 25 A. Batra, G. Kladnik, N. Gorjizadeh, J. Meisner, M. Steigerwald, C. Nuckolls, S. Y. Quek, D. Cvetko, A. Morgante and L. Venkataraman, *J. Am. Chem. Soc.*, 2014, **136**, 12556–12559.
- 26 W. Chen, J. R. Widawsky, H. Vazquez, S. T. Schneebeli, M. S. Hybertsen, R. Breslow and L. Venkataraman, *J. Am. Chem. Soc.*, 2011, **133**, 17160–17163.
- 27 Z. L. Cheng, R. Skouta, H. Vazquez, J. R. Widawsky, S. Schneebeli, W. Chen, M. S. Hybertsen, R. Breslow and L. Venkataraman, *Nat. Nanotechnol.*, 2011, **6**, 353–357.
- 28 L. Venkataraman, J. E. Klare, C. Nuckolls, M. S. Hybertsen and M. L. Steigerwald, *Nature*, 2006, **442**, 904–907.
- 29 S. Y. Quek, L. Venkataraman, H. J. Choi, S. G. Louie, M. S. Hybertsen and J. B. Neaton, *Nano Lett.*, 2007, **7**, 3477–3482.
- 30 M. Paulsson and M. Brandbyge, *Phys. Rev. B: Condens. Matter*, 2007, **76**, 115117.
- 31 I. V. Alabugin, K. M. Gilmore and P. W. Peterson, *Wiley Interdiscip. Rev.: Comput. Mol. Sci.*, 2011, **1**, 109–141.
- 32 J. Taylor, M. Brandbyge and K. Stokbro, *Phys. Rev. Lett.*, 2002, **89**, 138301.



Supporting Information

Controlling the Rectification Properties of Molecular Junctions through Molecule–Electrode Coupling

Matthieu Koepf, Christopher Koenigsmann, Wendu Ding, Arunbah Batra, Christian F.A. Negre, Latha Venkataraman, Gary W. Brudvig, Victor S. Batista, Charles A. Schmuttenmaer, and Robert H. Crabtree

Content

1. Synthesis and characterization of the <i>N</i> -phenylbenzamide (NPBA) derivatives	4
1.1 Reagents, solvents and glassware handling	4
1.2 Experimental procedures	5
2. Theoretical studies.....	14
2.1 Description of the leads	14
2.2 Representation of the density of State (DOS) for the different junctions	15
2.3 Representation of the eigenchannel computed at E_{NPBA} for each junction	16
2.4 Representation of the HOMO state distribution for the isolated NPBA backbone	16
2.5 Single-state tight-binding model	17
2.6 Angular dependence of the projected density of states of the phenyl and the Anchor-leads fragments $PDOS_{Ph}/PDOS_{Au-Anchor}$	19
3. NMR spectra	21
3.1 1H NMR spectra of 4'-methyl- <i>N</i> -methyl- <i>N</i> -(4-tolyl)benzamide in $CDCl_3$	21
3.2 ^{13}C NMR spectra of 4'-methyl- <i>N</i> -methyl- <i>N</i> -(4-tolyl)benzamide in $CDCl_3$	22
3.3 1H NMR spectra of 4'-bromomethyl- <i>N</i> -methyl- <i>N</i> -[4-(bromomethyl)phenyl]benzamide in CD_3CN	23
3.4 ^{13}C NMR spectra of 4'-bromomethyl- <i>N</i> -methyl- <i>N</i> -[4-(bromomethyl)phenyl]benzamide in CD_3CN	24
3.5 1H NMR spectra of 4'-(trimethylstannyl)methyl- <i>N</i> -methyl- <i>N</i> -[4((trimethylstannyl)-methylphenyl)]benzamide in CD_3OD	25
3.6 ^{13}C NMR spectra of 4'-(trimethylstannyl)methyl- <i>N</i> -methyl- <i>N</i> -[4((trimethylstannyl)-methylphenyl)]benzamide in CD_3OD	26
3.7 1H NMR spectra of 2[-4-(2',2',2'-trifluoroacetamido)phenyl]ethan-1-ol in $CDCl_3$	27
3.8 ^{19}F NMR spectra of 2[-4-(2',2',2'-trifluoroacetamido)phenyl]ethan-1-ol in $CDCl_3$	28
3.9 ^{13}C NMR spectra of 2[-4-(2',2',2'-trifluoroacetamido)phenyl]ethan-1-ol in $CDCl_3$	29
3.10 1H NMR spectra of 2,2,2-trifluoro-(4-(2-((tetrahydro-2 <i>H</i> -pyran-2-yl)oxy)ethyl)phenyl)acetamide in $CDCl_3$	30
3.11 ^{19}F NMR spectra of 2,2,2-trifluoro-(4-(2-((tetrahydro-2 <i>H</i> -pyran-2-yl)oxy)ethyl)phenyl)acetamide in $CDCl_3$	31
3.12 ^{13}C NMR spectra of 2,2,2-trifluoro-(4-(2-((tetrahydro-2 <i>H</i> -pyran-2-yl)oxy)ethyl)phenyl)acetamide in $CDCl_3$	32
3.13 1H NMR spectra of 2,2,2-trifluoro- <i>N</i> -methyl-(4-(2-((tetrahydro-2 <i>H</i> -pyran-2-yl)oxy)ethyl)-phenyl)acetamide in $CDCl_3$	33
3.14 ^{19}F NMR spectra of 2,2,2-trifluoro- <i>N</i> -methyl-(4-(2-((tetrahydro-2 <i>H</i> -pyran-2-yl)oxy)ethyl)-phenyl)acetamide in $CDCl_3$	34
3.15 ^{13}C NMR spectra of 2,2,2-trifluoro- <i>N</i> -methyl-(4-(2-((tetrahydro-2 <i>H</i> -pyran-2-yl)oxy)ethyl)-phenyl)acetamide in $CDCl_3$	35
3.16 1H NMR spectra of <i>N</i> -methyl-(4-(2-((tetrahydro-2 <i>H</i> -pyran-2-yl)oxy)ethyl)aniline in $CDCl_3$..	36

3.17 ¹³ C NMR spectra of <i>N</i> -methyl-4-(2-((tetrahydro-2 <i>H</i> -pyran-2-yl)oxy)ethyl)aniline in CDCl ₃	37
3.18 ¹ H NMR spectra of 4-(2-bromoethyl)- <i>N</i> -methyl- <i>N</i> -(4-(2-((tetrahydro-2 <i>H</i> -pyran-2-yl)oxy)ethyl)phenyl)benzamide in CDCl ₃	38
3.19 ¹³ C NMR spectra of 4-(2-bromoethyl)- <i>N</i> -methyl- <i>N</i> -(4-(2-((tetrahydro-2 <i>H</i> -pyran-2-yl)oxy)ethyl)phenyl)benzamide in CDCl ₃	39
3.20 ¹ H NMR spectra of 4-(2-bromoethyl)- <i>N</i> -methyl- <i>N</i> -(4-(2-bromoethyl)phenyl)benzamide in CDCl ₃	40
3.21 ¹³ C NMR spectra of 4-(2-bromoethyl)- <i>N</i> -methyl- <i>N</i> -(4-(2-bromoethyl)phenyl)benzamide in CDCl ₃	41
3.22 ¹ H NMR spectra of 4-(trimethylstannyl)ethyl- <i>N</i> -methyl- <i>N</i> -(4 ((trimethylstannyl)ethyl)phenyl)benzamide	42
3.23 ¹³ C NMR spectra of 4-(trimethylstannyl)ethyl- <i>N</i> -methyl- <i>N</i> -(4 ((trimethylstannyl)ethyl)phenyl)benzamide	43
4. References	44

1. Synthesis and characterization of the *N*-phenylbenzamide (NPBA) derivatives

1.1 Reagents, solvents and glassware handling

p-Tolylchloride, *N,N*-diisopropylethylamine, *N*-methyl-*p*-toluidine, *N*-bromosuccinimide, hexamethyldistannane, trifluoroacetic anhydride, *p*-toluenesulfonic acid, sodium hydride (60 wt-% dispersed in mineral oil), methyl iodide, ammonium chloride, oxalyl chloride, carbon tetrabromide, triphenylphosphine, and *n*-butyllithium (2.1M in hexanes) (reagents purity: 97-% or higher) were obtained from Alfa Aesar. 4-(*N,N*-dimethylamino)pyridine, triethylamine, 3,4-dihydro-2*H*-pyran and anhydrous potassium carbonate (K₂CO₃) (reagents purity: 97-% or higher) were obtained from Acros Organics. *Tetrakis*(triphenylphosphine)palladium(0), and copper(I)cyanide were purchased from Strem Chemicals. Benzoyl peroxide was purchased from Aldrich. 2-(Aminophenyl)ethanol was obtained from TCI America. All the reagents were used as received. For synthetic purposes dichloromethane (CH₂Cl₂, OmniSolv grade, EMD-Millipore) and tetrahydrofuran (THF, OmniSolv grade, non-stabilized, EMD-Millipore) were dried on a Pure Solv MD-5 solvent purification system (Innovative Technology) on activated aluminum oxide before use and were dispensed under nitrogen. Anhydrous benzene (Alfa Aesar DriSolv), methanol (MeOH, ACS grade, BDH), 200 proof ethanol (EtOH, Decon labs), and dimethylformamide (DMF, DriSolv grade, EMD-Millipore) were used as received. *N,N*-Diisopropylethylamine (DIPEA) and triethylamine (NEt₃) were distilled over potassium hydroxide (KOH) and stored under argon (Ar) before use. The glassware was oven-dried and cooled under nitrogen prior use. Anhydrous sodium sulfate (Na₂SO₄), sodium bicarbonate (NaHCO₃), citric acid, and sodium chloride (ACS grade) were obtained from JT-Baker. For purification purposes, dichloromethane (CH₂Cl₂, ACS grade, stabilized with amylenes, BDH), ethyl acetate (EtOAc, ACS grade, BDH), methanol (MeOH, ACS grade, BDH), hexanes (ACS grade, BDH) as well as toluene (ACS grade, Macron Fine Chemicals) were used

without further purification. For nuclear magnetic resonance studies (NMR), deuterated acetonitrile (CD₃CN containing 0.05 v/v-% of tetramethylsilane (TMS)), deuterated methanol (CD₃OD) and deuterated chloroform (CDCl₃, containing 0.05% v/v-% TMS) were obtained from Cambridge Isotope Laboratory.

Analytical thin layer chromatography (TLC) was conducted on glass-coated silica gel 60 F254 plates obtained from EMD-Millipore. Column chromatography were conducted on silica gel (SiO₂, 43–60 μm or 18–22 μm) provided by Silicycle. Unless otherwise specified, the 43–60 μm silica gel was used as stationary phase for the columns. Celite® 545 was purchased from EMD-Millipore. NMR spectra were recorded on a Varian DPX spectrometer coupled to an Oxford 400 magnet. ¹H spectra were recorded at 400 MHz, and ¹³C NMR at 101 MHz. Chemical shifts are reported according to TMS as the internal reference. High resolution mass spectrometry was performed on an Agilent G6550A Q-TOF LC/MS with API by direct injection, otherwise the sample were run on a an Agilent-1260 Infinity(LC)/6120B(MS) system using a C18 column (1.8 μm, 4.6 x 50 mm); in all cases the compounds were dissolved in methanol at an approximate concentration of 0.5 mg/mL. All the NPBA derivatives were stored under Ar at -20°C.

1.2 Experimental procedures

Synthesis and full characterization of NH₂-NPBA derivative has been described elsewhere.¹

Synthesis of 4'-methyl-N-methyl-N-(4-tolyl)benzamide

p-Tolylchloride (4.78 g, 30.9 mmol) was dissolved in anhydrous dichloromethane (40 mL). *N,N*-dimethyl-4-aminopyridine (0.62 g, 5.15 mmol) and dry *N,N*-diisopropylethylamine (6.9 ml, 5.16 g, 40 mmol) were added under nitrogen. *N*-Methyl-*p*-toluidine (2.6 mL, 2.5 g, 20.6 mmol) was added dropwise over a period of 5 minutes and the mixture was refluxed under nitrogen for 2 hours. TLC analysis (SiO₂, CH₂Cl₂) indicated that all the *N*-methyl-*p*-toluidine was converted. The mixture was extracted with 5% aqueous NaHCO₃ (2 x 100 mL), 5% aqueous citric acid (2 x 100 mL) and water (100 mL). The organic layer was dried over

Na₂SO₄, filtered, and the solvent was evaporated. Column chromatography (SiO₂, CH₂Cl₂ 1%- EtOAc) yielded the desired product as an off-white solid (5.01 g, 20.1 mmol, 98%).

¹H-NMR (400 MHz, CDCl₃) δ 7.20 (d, *J* = 8.1 Hz, 2H), 7.02 (d, *J* = 8.0 Hz, 2H), 6.96 (d, *J* = 8.0 Hz, 2H), 6.91 (d, *J* = 8.3 Hz, 2H), 3.45 (s, 3H), 2.28 (s, 3H), 2.26 (s, 3H).

¹³C-NMR (101 MHz, CDCl₃) δ 170.63, 142.62, 139.59, 136.09, 133.06, 129.71, 128.84, 128.30, 126.61, 38.56, 21.31, 20.93.

MS (m/z 100%) calc. for C₁₆H₁₇NO+H⁺: 240.1; found 240.2.

Synthesis of 4'-bromomethyl-*N*-methyl-*N*-[4-(bromomethyl)phenyl]benzamide

4-methyl-*N*-methyl-*N*-(4-tolyl)benzamide (2g, 8.56 mmol) was dissolved in anhydrous benzene (10 mL) under nitrogen. The mixture was purged with nitrogen (vacuum-nitrogen cycles, 3x) and brought to 80 °C under nitrogen. *N*-bromosuccinimide (2.97 g, 16.72 mmol) and benzoyl peroxide (387 mg, 1.6 mmol) were added and the mixture was stirred under gentle reflux for 1 hour under nitrogen. TLC analysis (SiO₂, toluene 5%-EtOAc) indicated full conversion of the starting material. The solution was cooled down to room temperature and the solid filtered out and washed with toluene (3 x 30 mL). The solvent was evaporated and the crude was purified by column chromatography (SiO₂ hexanes-20% EtOAc, 5th band collected). The obtained product contained a minor impurity that was eliminated by running a second column chromatography (SiO₂, CH₂Cl₂ 1%-EtOAc, 2nd band collected). The desired compound was obtained as a white solid (1.5 g, 3.78 mmol, 44%).

¹H-NMR (400 MHz, CD₃CN) δ 7.31 (d, *J* = 8.4 Hz, 2H), 7.27 (br s, 4H), 7.12 (d, *J* = 8.4 Hz, 2H), 4.51 (s, 2H), 4.49 (s, 2H), 3.38 (s, 3H).

¹³C-NMR (101 MHz, CD₃CN) δ 169.49, 144.85, 139.67, 136.65, 129.86, 128.82, 128.51, 127.45, 37.62, 32.81, 32.70.

MS (m/z 100%) calc. for C₁₆H₁₅Br₂NO+H⁺: 397.9; found 397.8.

Synthesis of 4'-(trimethylstannyl)methyl-*N*-methyl-*N*-[4((trimethylstannyl)methylphenyl)]benzamide

4'-bromomethyl-*N*-methyl-*N*-[4-(bromomethyl)phenyl]benzamide (199 mg, 0.5 mmol) and melted hexamethyldistannane (0.4 mL, 632 mg, 1.9 mmol) were dissolved in anhydrous toluene (20 mL) and the mixture was purged with argon (vacuum/argon cycles, 3x). Tetrakis(triphenylphosphine)palladium(0) (12 mg, 10 μ mol) was added and the mixture purged with argon (vacuum/argon cycles, 3x) and stirred at 90 °C under argon for 12 hours. TLC analysis (SiO₂, CH₂Cl₂-2% EtOAc) indicated that the reaction was complete. The mixture was filtered over Celite® to remove the precipitated solid and the solvent was evaporated. The crude material was purified by column chromatography (SiO₂, CH₂Cl₂-1% EtOAc). The second band contained the desired product. It was collected and the solvent was evaporated. A second column chromatography (SiO₂ hexanes-20% EtOAc) yielded the pure 4'-(trimethylstannyl)methyl-*N*-methyl-*N*-[4((trimethylstannyl)methylphenyl)] benzamide (second product collected) as a white solid (176 mg, 0.31 mmol, 62%).

¹H-NMR (400 MHz, CD₃OD) δ 7.08 (d, J = 8.3 Hz, 2H), 6.95 – 6.82 (m, 4H), 6.78 (d, J = 7.8 Hz, 2H), 3.41 (s, 3H), 2.40 – 2.12 (m, 4H), 0.20 – -0.21 (m, 18H).

¹³C-NMR (101 MHz, CD₃OD) δ 171.79, 146.06, 142.37, 140.06, 130.28, 128.60, 126.98, 126.57, 125.54, 37.41, 19.73, 19.00, -11.68, -11.72.

HRMS (m/z 100%) calc. for C₂₂H₃₃NOSn₂+H⁺: 566.0673; found 566.0670.

Synthesis of 2-[4-(2',2',2'-trifluoroacetamido)phenyl]ethyl-2'',2'',2''-trifluoroacetate

2-(4-aminophenyl)ethanol (288 mg, 2.1 mmol) was dissolved in anhydrous dichloromethane (50 mL). K₂CO₃ (1.38 g, 10 mmol) was added followed by trifluoroacetic anhydride (0.84 mL, 1.26 g, 6 mmol) and the mixture was stirred at room temperature, under nitrogen for 1 hour. TLC analysis (SiO₂, CH₂Cl₂) confirmed that the reaction was complete and the mixture was filtered to remove the solid. The organic layer was washed with water (3

x 50 mL), collected dried on Na₂SO₄ filtered and the solvent was evaporated to yield the desired compound as a white solid (635 mg, 1.9 mmol, 92%). The compound was used for the next step without further purification.

Due to the fast hydrolysis of the trifluoroacetate ester, traces of the free alcohol were observed in NMR spectroscopy.

Synthesis of 2[-4-(2',2',2'-trifluoroacetamido)phenyl]ethan-1-ol

2-[4-(2',2',2'-trifluoroacetamido)phenyl]ethyl-2'',2'',2''-trifluoroacetate (635 mg, 1.9 mmol) was dissolved in methanol (50 mL) and 9 μ L of a 2.3 M aqueous solution of potassium hydroxide (20 μ mol) was added and the mixture was stirred at 50 °C, under nitrogen, for 1 hour. TLC analysis (SiO₂, hexanes-20% EtOAc) confirmed the full conversion of the starting material. The solution was cooled down to room temperature, and the solvent was evaporated under reduced pressure to yield the desired product as a white solid (446 mg, quant.). It was used for the next reaction without further purification.

¹H NMR (400 MHz, CDCl₃) δ 7.86 (br. s, 1H), 7.51 (d, *J* = 8.5 Hz, 2H), 7.25 (d, *J* = 8.5 Hz, 2H), 3.86 (t, *J* = 6.5 Hz, 2H), 2.88 (t, *J* = 6.5 Hz, 2H).

¹⁹F NMR (376 MHz, CDCl₃) δ -75.72.

¹³C NMR (101 MHz, CDCl₃) δ 136.95, 133.44, 129.91, 120.70, 63.45, 38.57.

MS analysis did not show the expected molecular ion of the alcohol derivative (C₁₀H₁₀F₃NO₂+H⁺) but the product of acid catalyzed dehydration was observed:

MS (m/z 100%) calc. for C₁₀H₈F₃NO+H⁺: 248.1; found 248.0.

Synthesis of 2,2,2-trifluoro-(4-(2-((tetrahydro-2H-pyran-2-yl)oxy)ethyl)phenyl)acetamide

2[-4-(2',2',2'-trifluoroacetamido)phenyl]ethan-1-ol was dissolved in anhydrous dichloromethane (50 mL), 3,4-dihydro-2H-pyran (200 μ L, 192 mg, 2.28 mmol) was added followed by *p*-toluenesulfonic acid (19 mg, 0.1 mmol). The mixture was stirred under nitrogen, at room temperature. After 4 hours, TLC analysis (SiO₂, hexanes-10% EtOAc)

indicated full conversion of the starting material. The mixture was extracted with 5%-aqueous NaHCO₃ (2 x 50 mL) and water (1 x 50 mL). The organic layer was collected, dried over Na₂SO₄, filtered and the solvent was evaporated under reduced pressure. The crude residue was purified by column chromatography (SiO₂, hexanes-10% EtOAc) to yield the desired compound as a clear oil (655.2 mg, 2.06 mmol, 91%).

¹H NMR (400 MHz, CDCl₃) δ 7.84 (br. s, 1H), 7.48 (d, *J* = 8.5 Hz, 2H), 7.27 (d, *J* = 8.5 Hz, 2H), 4.58 (dd, *J*₁ = 4.2 Hz, *J*₂ = 2.8 Hz, 1H), 3.94 (dt, *J*₁ = 9.7 Hz, *J*₂ = 7.0 Hz, 1H), 3.77 – 3.71 (m, 1H), 3.60 (dt, *J*₁ = 9.7 Hz, *J*₂ = 6.9 Hz, 1H), 3.48 – 3.43 (m, 1H), 2.90 (t, *J* = 7.0 Hz, 2H), 1.82 – 1.72 (m, 1H), 1.75 – 1.64 (m, 1H), 1.63 – 1.42 (m, 4H).

¹⁹F NMR (376 MHz, CDCl₃) δ -75.73.

¹³C NMR (101 MHz, CDCl₃) δ 137.67, 133.15, 129.88, 120.37, 98.75, 67.92, 62.19, 35.79, 30.62, 25.41, 19.45.

MS (m/z 100%) calc. for C₁₅H₁₈F₃NO₃+Na⁺: 340.1; found 340.0.

Synthesis of 2,2,2-trifluoro-*N*-methyl-(4-(2-((tetrahydro-2*H*-pyran-2-yl)oxy)ethyl) phenyl acetamide

2,2,2-trifluoro-(4-(2-((tetrahydro-2*H*-pyran-2-yl)oxy)ethyl)phenyl)acetamide (607 mg, 1.9 mmol) was dissolved in anhydrous THF (25 mL) under nitrogen. sodium hydride (60 wt-% dispersion in mineral oil, 87 mg, 2.18 mmol) was added and the reaction mixture was stirred under nitrogen, at room temperature, for 5 minutes. Methyl iodide (200 μL, 456 mg, 3.2 mmol) was added and the mixture was stirred at 45 °C, under nitrogen. The progression of the reaction was followed by TLC analysis (SiO₂, hexanes-10% EtOAc). After 2 hours complete conversion of the starting material was observed. The mixture was cooled down to room temperature and quenched with a saturated solution of aqueous ammonium chloride (1 mL). The mixture was poured into a 5% aqueous NaHCO₃ solution (100 mL). The aqueous layer was extracted with ethyl acetate (2 x 50 mL). The combined organic layers were then washed

with a 5% aqueous solution of NaHCO₃ (100 mL) and water (100 mL). The organic layer was collected, dried over Na₂SO₄, filtered and the solvent was evaporated under reduced pressure. Column chromatography (SiO₂, hexanes-10% EtOAc) yield the desired compound as a colorless oil. ¹H-NMR showed that it was 90% pure containing some *N,N*-dimethyl-(4-(2-((tetrahydro-2*H*-pyran-2-yl)oxy)ethyl)aniline. It was use without further purification in the next step. Yield: 591 mg, 1.78 mmol, 94%.

¹H NMR (400 MHz, CDCl₃) δ 7.31 (d, *J* = 8.3 Hz, 2H), 7.15 (d, *J* = 8.3 Hz, 2H), 4.60 – 4.58 (m, 1H), 3.94 (dt, *J*₁ = 9.7 Hz, *J*₂ = 7.0 Hz, 1H), 3.66 – 3.60 (m, 2H), 3.52 – 3.39 (m, 1H), 3.34 (s, 3H), 2.94 (t, *J* = 7.0 Hz, 2H), 1.88 – 1.63 (m, 2H), 1.63 – 1.43 (m, 4H).

¹⁹F NMR (376 MHz, CDCl₃) δ -67.10.

¹³C NMR (101 MHz, CDCl₃) δ 140.56, 130.11, 127.09, 98.55, 67.60, 61.98, 39.69, 35.91, 30.57, 29.68, 25.38, 19.31.

MS (m/z 100%) calc. for C₁₆H₂₀F₃NO₃+H⁺: 332.2; found 332.2.

Synthesis of *N*-methyl-(4-(2-((tetrahydro-2*H*-pyran-2-yl)oxy)ethyl)aniline

2,2,2-trifluoro-*N*-methyl- (4-(2-((tetrahydro-2*H*-pyran-2-yl)oxy)ethyl)phenylacetamide (570 mg, 1.72 mmol) was dissolved in methanol (25 mL). Potassium hydroxide (250 mg, 4.45 mmol) dissolved in 1 mL of water was added and the mixture was purged with nitrogen (vacuum nitrogen cycles, 3x). The mixture was stirred at room temperature, under nitrogen, for 3 hours. TLC analysis (SiO₂, toluene-10% EtOAc) indicated complete conversion of the starting material. The solvent was evaporated to 5 mL and the mixture diluted to 50 mL with EtOAc. The organic layer was extracted with brine (3 x 50 mL), collected, dried over Na₂SO₄, filtered and the solvent was evaporated to yield the desired aniline as a colorless oil (404 mg, 1.72 mmol, quant.). The aniline was used without further purification in the following step.

¹H NMR (400 MHz, CDCl₃) δ 7.06 (d, *J* = 8.4 Hz, 2H), 6.56 (d, *J* = 8.4 Hz, 2H), 4.59 (dd, *J*₁ = 4.4 Hz, *J*₂ = 2.9 Hz, 1H), 3.89 (dt, *J*₁ = 9.7 Hz, *J*₂ = 7.4 Hz, 1H), 3.82 – 3.78 (m, 1H), 3.56 (dt, *J*₁ = 9.7 Hz, *J*₂ = 7.4 Hz, 1H), 3.51 – 3.42 (m, 1H), 2.82 (s, 3H), 2.81 (t, *J* = 7.0 Hz, 2H), 1.88 – 1.77 (m, 1H), 1.76 – 1.64 (m, 1H), 1.64 – 1.44 (m, 4H).

¹³C NMR (101 MHz, CDCl₃) δ 147.66, 129.68, 127.68, 112.52, 98.73, 68.83, 62.24, 35.45, 30.99, 30.72, 25.49, 19.58.

MS (m/z 100%) calc. for C₁₄H₂₁NO₂+H⁺: 236.2; found 236.2.

Synthesis of 4-(2-bromoethyl)-*N*-methyl-*N*-(4-(2-((tetrahydro-2*H*-pyran-2-yl)oxy)ethyl)-phenyl)benzamide

4-(2-bromoethyl)benzoic acid (690 mg, 3mmol) was suspended in anhydrous benzene (30 mL) under nitrogen. Oxalyl chloride (326 μL, 474 mg, 3.75 mmol) was added followed by a drop of anhydrous dimethylformamide (5 μL). The mixture was stirred at room temperature, under nitrogen for 3 hours. The solvent was reduced to 10 mL and anhydrous triethylamine (1.2 mL, 0.859 mg, 8.5 mmol) was added, followed by a solution of *N*-methyl-4-(2-((tetrahydro-2*H*-pyran-2-yl)oxy)ethyl)aniline (400 mg, 1.7 mmol) in anhydrous dichloromethane (6 mL) and *N,N*-dimethylaminopyridine (25 mg, 0.2 mmol). The mixture was further stirred under nitrogen, at room temperature for 12 hours. The mixture was diluted to 100 mL with dichloromethane and extracted with 5% aqueous NaHCO₃ (2 x 100 mL) and water (100 mL). The organic layer was collected, dried over Na₂SO₄, filtered and the solvent was evaporated. The crude residue was purified by column chromatography (SiO₂, CH₂Cl₂-6% EtOAc) to yield the desired compound as a colorless oil (618 mg, 1.3 mmol, 81%).

¹H NMR (400 MHz, CDCl₃) δ 7.25 (d, *J* = 8.1 Hz, 2H), 7.10 (d, *J* = 8.3 Hz, 2H), 7.00 (d, *J* = 8.1 Hz, 2H), 6.94 (d, *J* = 8.3 Hz, 2H), 4.56 – 4.54 (m, 1H), 3.88 (dt, *J*₁ = 9.7 Hz, *J*₂ = 7.1 Hz, 1H), 3.75 – 3.69 (m, 1H), 3.55 (dt, *J*₁ = 9.7 Hz, *J*₂ = 7.0 Hz, 1H), 3.52 – 3.39 (m, 6H), 3.07 (t, *J* = 7.6 Hz, 2H), 2.84 (t, *J* = 7.1 Hz, 2H), 1.80 – 1.75 (m, 1H), 1.70 – 1.65 (m, 1H), 1.58 – 1.48 (m, 4H).

¹³C NMR (101 MHz, CDCl₃) δ 170.29, 142.99, 140.34, 137.63, 134.61, 129.71, 129.08, 127.95, 126.63, 98.70, 67.91, 62.17, 39.03, 38.50, 35.74, 32.20, 30.60, 25.41, 19.45.

MS (m/z 100%) calc. for C₂₃H₂₈BrNO₃+H⁺: 446.1; found 446.0.

Synthesis of 4-(2-bromoethyl)-*N*-methyl-*N*-(4-(2-bromoethyl)phenyl)benzamide

4-(2-bromoethyl)-*N*-methyl-*N*-(4-(2-((tetrahydro-2*H*-pyran-2-yl)oxy)ethyl)phenyl)benzamide (100 mg, 0.22 mmol) was dissolved in anhydrous dichloromethane (2.5 mL), carbon tetrabromide (97 mg, 0.29 mmol) was added and the mixture stirred at room temperature, under nitrogen, for 10 minutes before being cooled down to 0 °C. Triphenylphosphine (153 mg, 0.58 mmol) was added and the mixture was stirred at 0 °C, under nitrogen, for 1 hour then allowed to warm up to room temperature. The mixture was further stirred at room temperature for 2 hours after which time TLC analysis (SiO₂, CH₂Cl₂-10% EtOAc) showed that all the starting material reacted. The crude mixture was purified by column chromatography (SiO₂, CH₂Cl₂-10% EtOAc) to yield the desired product as a colorless oil (93 mg, 0.22 mmol, 98%).

¹H NMR (400 MHz, CDCl₃) δ 7.24 (d, *J* = 8.1 Hz, 2H), 7.07 (d, *J* = 8.3 Hz, 2H), 7.01 (d, *J* = 8.2 Hz, 2H), 6.98 (d, *J* = 8.3 Hz, 2H), 3.52 – 3.44 (m, 7H), 3.11 – 3.05 (m, 4H).

¹³C NMR (101 MHz, CDCl₃) δ 170.27, 143.63, 140.45, 137.16, 134.45, 129.39, 129.08, 128.01, 126.93, 38.99, 38.56, 38.37, 32.67, 32.31.

MS (m/z 100%) calc. for C₁₈H₁₉Br₂NO+H⁺: 426.0; found 426.0.

Synthesis of 4-(trimethylstannyl)ethyl-*N*-methyl-*N*-(4-((trimethylstannyl)ethyl)phenyl)benzamide

Copper cyanide (68 mg, 0.76 mmol) was suspended in oxygen free, anhydrous THF. The suspension was purged with argon (vacuum argon cycles, 3 cycles) and cooled down to -40 °C using an acetonitrile-dry ice cooling bath. *n*-Buthyllithium (680 μL, 2.2 M in hexanes, 0.15mmol) was added dropwise to the suspension and the mixture was stirred at -40 °C for 30 minutes, under argon. Hexamethyldistannane (146 μL, 231 mg, 0.71 mmol) was added dropwise and the mixture was further stirred at -40 °C for 1 hour under argon. The cuprate solution was then cooled down to -78 °C (acetone/dry ice bath) and an oxygen-free solution of 4-(2-bromoethyl)-*N*-methyl-*N*-(4-(2-bromoethyl)phenyl)benzamide (100 mg, 0.23 mmol) dissolved in anhydrous THF (5 mL) was transferred dropwise to the cold cuprate slurry (addition time ca. 5 minutes) via a cannula. The mixture was further stirred at -78 °C for 15 minutes, then stirred at -40 °C for 15 minutes and was then slowly allowed to warm up to 0 °C and stirred at 0 °C, another 30 minutes, under argon. The reaction was quenched with a saturated aqueous solution of ammonium chloride (5 mL). The mixture was poured into hexanes (100 mL) and the organic phase was then washed with saturated aqueous ammonium chloride (2 x 50 mL) and water (1 x 50 mL). The organic layer was collected, dried over Na₂SO₄, filtered and the solvent was evaporated. The crude residue was purified by column chromatography (SiO₂, 18 – 22 μm, toluene-5% EtOAc) to yield the desired compound (32.1 mg, 54 μmol, 23%, first eluted band) as a white solid.

¹H NMR (400 MHz, CDCl₃) δ 7.22 (d, *J* = 7.9 Hz, 2H), 7.03 (d, *J* = 8.1 Hz, 2H), 6.97 (d, *J* = 8.0 Hz, 2H), 6.93 (d, *J* = 8.1 Hz, 2H), 3.46 (s, 3H), 2.91 – 2.54 (m, 4H), 1.08 (h, *J* = 7.7 Hz, 4H), 0.23 – -0.32 (m, 18H).

¹³C NMR (101 MHz, CDCl₃) δ 170.64, 146.83, 143.36, 142.84, 133.27, 129.02, 128.51, 127.15, 126.68, 38.59, 32.36, 32.01, 12.21, 12.03, -10.21.

HRMS (m/z 100%) calc. for C₂₄H₃₇NOSn₂+H⁺: 594.0986; found 594.0986.

2. Theoretical studies

2.1 Description of the leads

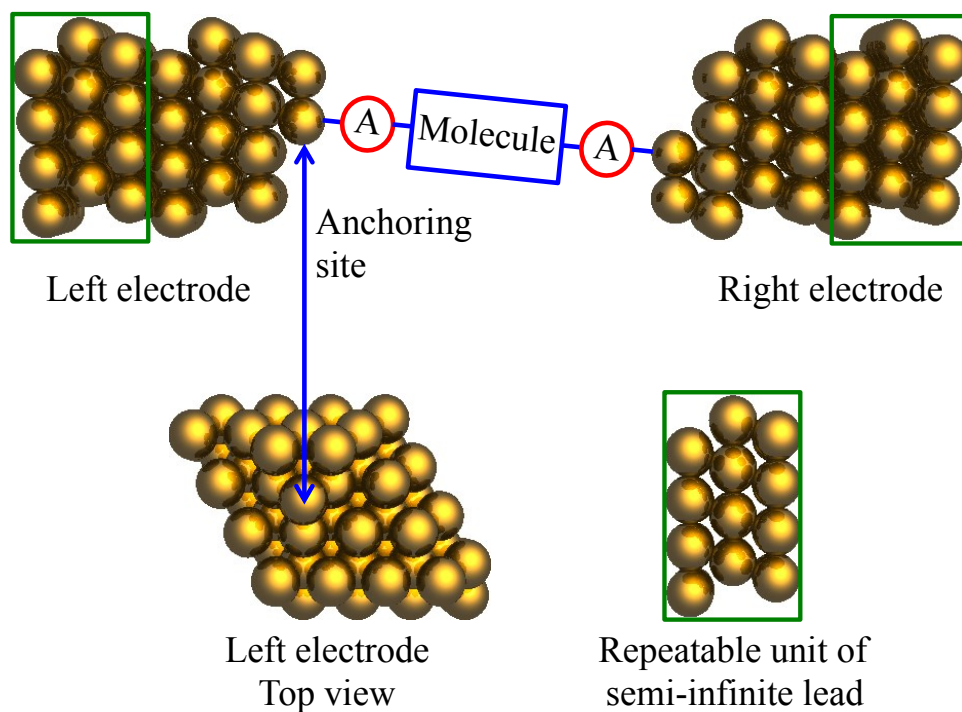


Figure S1. Representation of the gold electrodes used in I-V curve calculations. They consist of 6 layers of 16 gold atoms cut from an Au fcc lattice, with a triad contact motif attached to the (111) surface. The lattice constant is 4.080 Å.

2.2 Representation of the density of State (DOS) for the different junctions

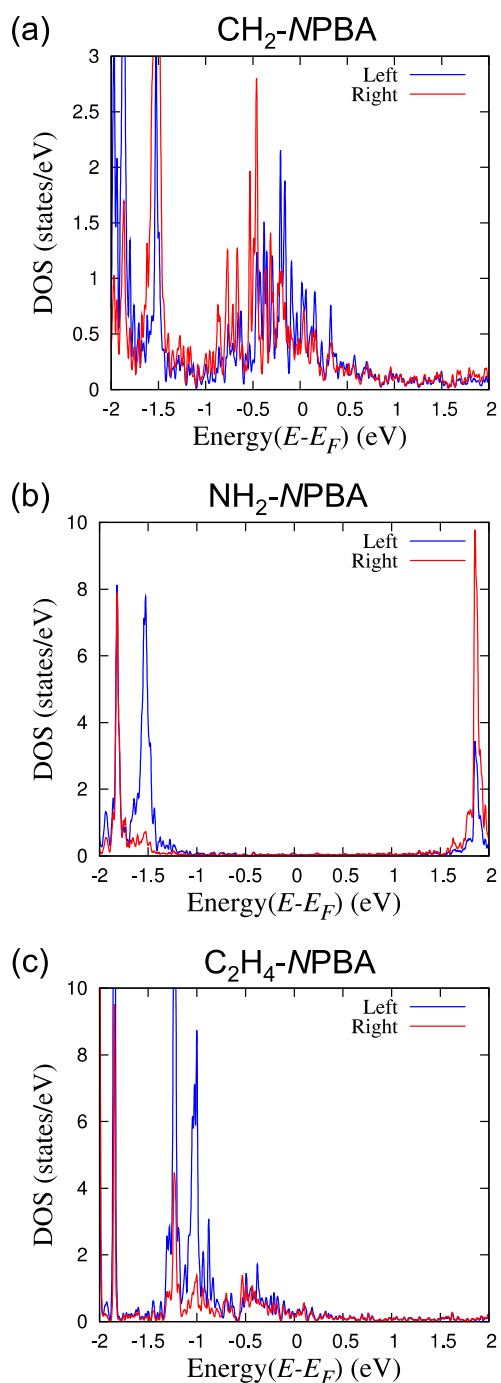


Figure S2. Representation of the density of states for all three molecules. Blue line (labeled Left) indicates states localized on the left-hand side of the molecule, while red line (labeled Right) indicates states localized on the right-hand side of the molecule. Left and right sides are determined with respect to the central amide bond and systematically using the -PhNMeCOPh- orientation.

2.3 Representation of the eigenchannel computed at E_{NPBA} for each junction

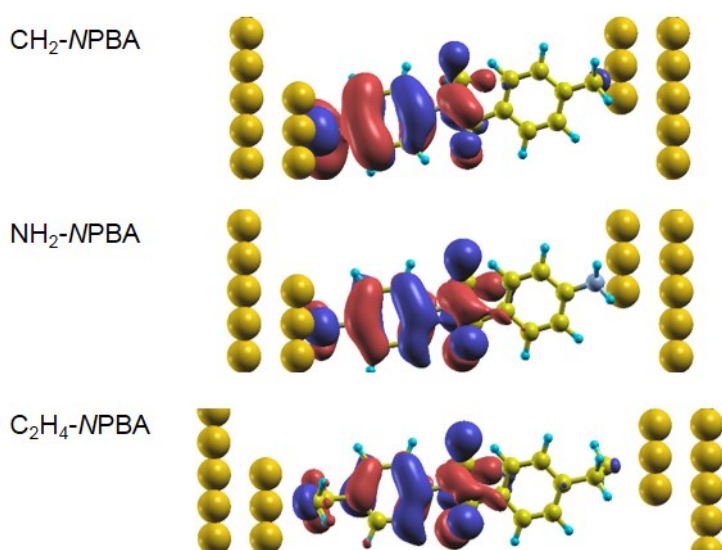


Figure S3. Representation of the eigenchannel at E_{NPBA} for each junction. Note the clear homology between the eigenchannels of the three junctions. Since the eigenchannel represents the principal eigenvector of the transmission matrix it gives a picture of the orbitals involved in the electron transport through the junction.

2.4 Representation of the HOMO state distribution for the isolated NPBA backbone

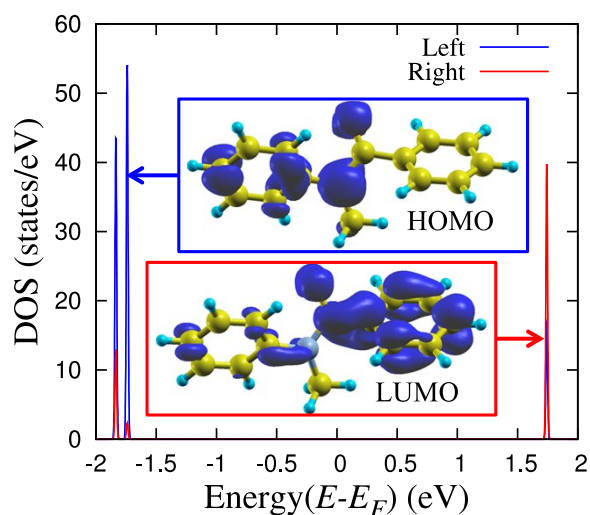


Figure S4. Representation of the density of states of an isolated NPBA molecule determined using GGA-PBE functional as implemented in SIESTA. Insets are LDOS plots for HOMO and LUMO states.

2.5 Single-state tight-binding model

In order to introduce the effect of applying a bias across the molecule, we have used a single-state tight-binding model, as described in details in a previous publication.¹ In this model the molecule is approximated as a single state, coupled to two electron reservoirs (electrodes). For such a system, the transmission function under a certain applied bias, $T(\varepsilon, V)$, can be described by the Breit-Wigner formula:²

$$T(\varepsilon, V) = \frac{4\Gamma_L \Gamma_R}{\left[\varepsilon - \varepsilon_0(V)\right]^2 + (\Gamma_L + \Gamma_R)^2} \quad \text{Eq. S1}$$

where ε_0 is the energy of the isolated state, Γ_L and Γ_R are the left and right coupling to the electrodes, respectively. Based on previous studies,³⁻⁴ low-bias rectification is caused by the energy shifting of the frontier orbital of the molecule; translating into this model, it means that the rectification can be approximated by the asymmetric shifting of ε_0 due to the applied bias. Here, we used the HOMO of the molecule as the single state ε_0 . This state will be spatially localized at the “centroid” of HOMO (see **Figure S5**). The bias-induced shifting of ε_0 is determined by the following equation:

$$\varepsilon_0(V) = \varepsilon_0(0) + V \times \frac{\text{state-lead distance}}{\text{junction length}} \quad \text{Eq. S2}$$

where V is the applied bias. The junction length is the distance between the two gold contacts. The state-lead distance is the distance between the state ε_0 (at the center of mass of HOMO) and the geometric center of the junction in the transport direction. Therefore, the transmission function under different bias can be approximated by substituting **Eq. S2** into **Eq. S1** to give:

$$T(\varepsilon, V) = \frac{4\Gamma_L \Gamma_R}{\left\{ \varepsilon - \left[\varepsilon_0(0) + V \times \frac{\text{state-lead distance}}{\text{junction length}} \right] \right\}^2 + (\Gamma_L + \Gamma_R)^2} \quad \text{Eq. S3}$$

The values of $\varepsilon_0(0)$, Γ_L , and Γ_R can be obtained by fitting the dominant transmission peak using **Eq. S1**, setting these three quantities as parameters. These quantities, together with state-lead distance and junction length, are shown in **Table S1**. As one can see, the RMSE (root-mean-squared error) for all three fits are sufficiently small, indicating less than 1% error between the fitted T and the T calculated as described in the Methods section in main text. Once these parameters are obtained, the transmission function of the dominant transport channel under different biases can be calculated using **Eq. S3**, and in turn the current under those biases by integrating the transmission function. Finally, the rectification ratio can be obtained by taking the ratio of the currents between the positive and negative biases.

Table S1. Parameters from zero-bias transmission function fitted by **Eq. S1**.

Molecule	$\varepsilon_0(0)$ (eV)	Γ_L (eV)	Γ_R (eV)	RMSE (%)	State-lead distance (Å)	Junction length (Å)
CH ₂ -NPBA	-0.286	-0.2304	-0.0091	0.63	3.0192	14.4349
NH ₂ -NPBA	-1.580	-0.0298	-0.0008	0.14	1.2623	14.3949
C ₂ H ₄ -NPBA	-1.110	-0.0322	-0.0024	0.12	0.5187	17.6785

Note: the Gamma values (Γ_L , Γ_R) obtained indicate an asymmetric coupling of the molecular state (gateway orbital) with the leads, which is translated into TF peaks that attain only fractional values of the quantum unit of conductance.

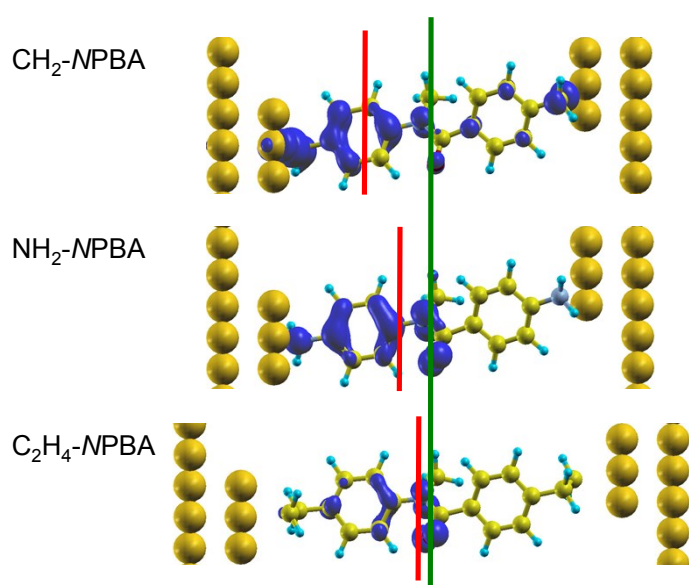


Figure S5. Representation of the isosurfaces of the LDOS for **CH₂-NPBA**, **NH₂-NPBA**, and **C₂H₄-NPBA** at E_{NPBA} . The green and red lines are the projections of the planes that are perpendicular to the transport direction and that include the geometric center of the junction, and the centroid of the HOMO-derived electronic state, respectively.

2.6 Angular dependence of the projected density of states of the phenyl and the Anchor-leads fragments $\text{PDOS}_{\text{Ph}}/\text{PDOS}_{\text{Au-Anchor}}$

To quantify the effects of the different anchoring groups on the electronic coupling between the gold leads and the π -system of the NPBA backbone, we calculated the ratio of the projected density of states (PDOS) of the phenyl fragment (PDOS_{Ph}) to the adjacent lead–anchor motif ($\text{PDOS}_{\text{Au-Anchor}}$) for both **CH₂-NPBA** and **NH₂-NPBA**, with different dihedral angles between the Au–anchor and phenyl ring (see **Figure S6**, which uses **NH₂-NPBA** as an example). We considered rotations of the phenyl plane by +0°, +30°, +60° and +90° relative to the initial (equilibrium) geometry. The density of states distribution is different for **CH₂-NPBA** and **NH₂-NPBA**, therefore, for a fair comparison, the ratio $\text{PDOS}_{\text{Ph}}/\text{PDOS}_{\text{Au-Anchor}}$ calculated for the molecules with same anchoring groups are normalized to the lowest value within the series. In the case of **CH₂-NPBA**, the normalization factor is the ratio obtained for the equilibrium geometry (+0°), while in the case of **NH₂-NPBA**, it is the ratio calculated with an increment of +60° relative to the equilibrium geometry. The results are shown in **Table S2** and **Figure S7**. As can be seen, the PDOS ratio changes dramatically in the case of **CH₂-NPBA**, with a 7-fold increase of the normalized value, within the series. Meanwhile, the PDOS ratio for **NH₂-NPBA** only exhibits a 2-fold decrease through the series.

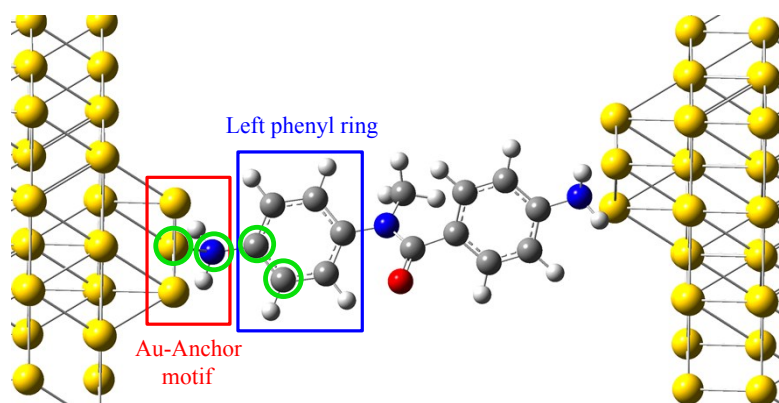


Figure S6. Definition of the regions named Au–Anchor motif and left phenyl ring. The dihedral angle between the Au–anchor and phenyl ring is defined by the atoms labeled with the green circles in the figure. The figure depicts the initial geometry of the NPBA in the junction (+ 0°).

Table S2. PDOS ratios between left phenyl ring and the anchor–Au motif ($\text{PDOS}_{\text{Ph}}/\text{PDOS}_{\text{Au-Anchor}}$), after rotation of phenyl ring plane from its original position by the specified angular increment.

Molecule	+ 0°	+ 30°	+ 60°	+ 90°
CH ₂ -NPBA	1.00	2.52	4.64	7.19
NH ₂ -NPBA	1.74	1.20	1.00	1.00

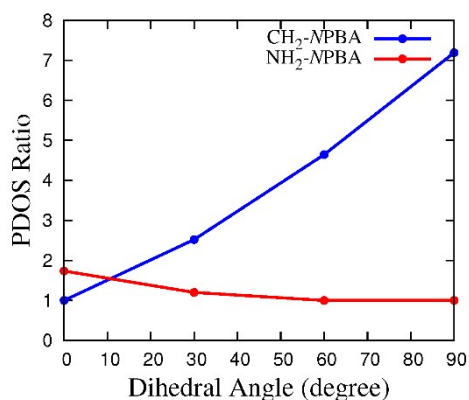
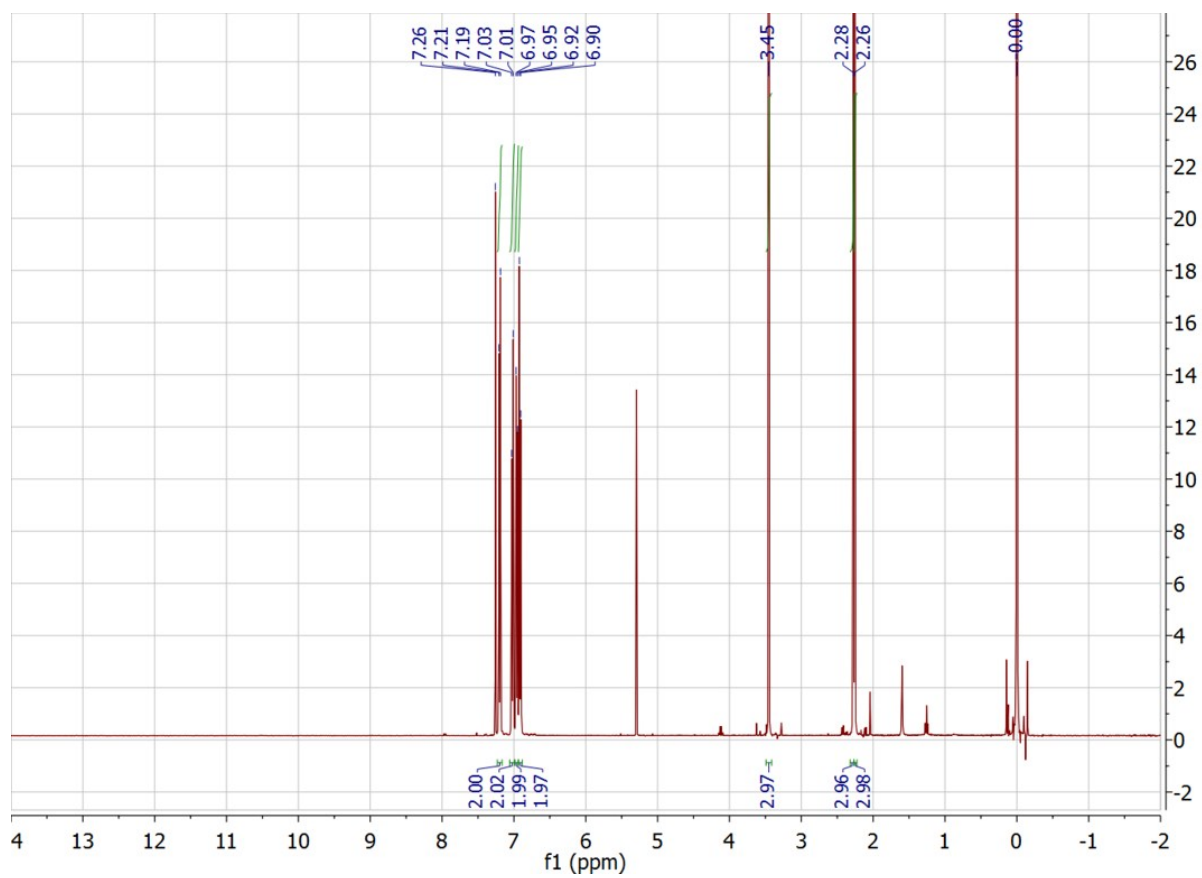


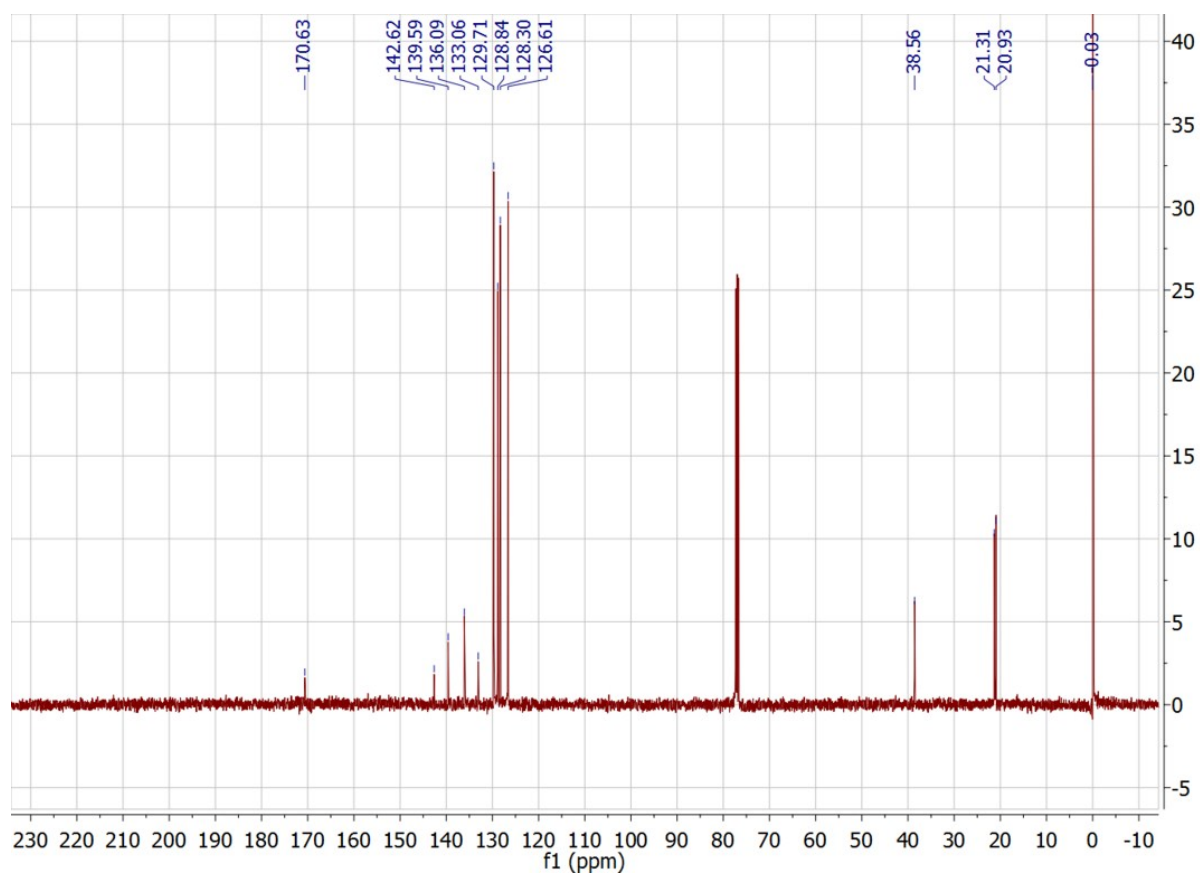
Figure S7. Evolution of the ratio $\text{PDOS}_{\text{Ph}}/\text{PDOS}_{\text{Au-Anchor}}$ as a function of the dihedral angle between the left phenyl ring and the anchor–Au motif for CH₂-NPBA and NH₂-NPBA. The values indicated (+0°, +30°, +60°, +90°) correspond to the incremental rotation of the phenyl ring plane from its original (relaxed) position.

3. NMR spectra

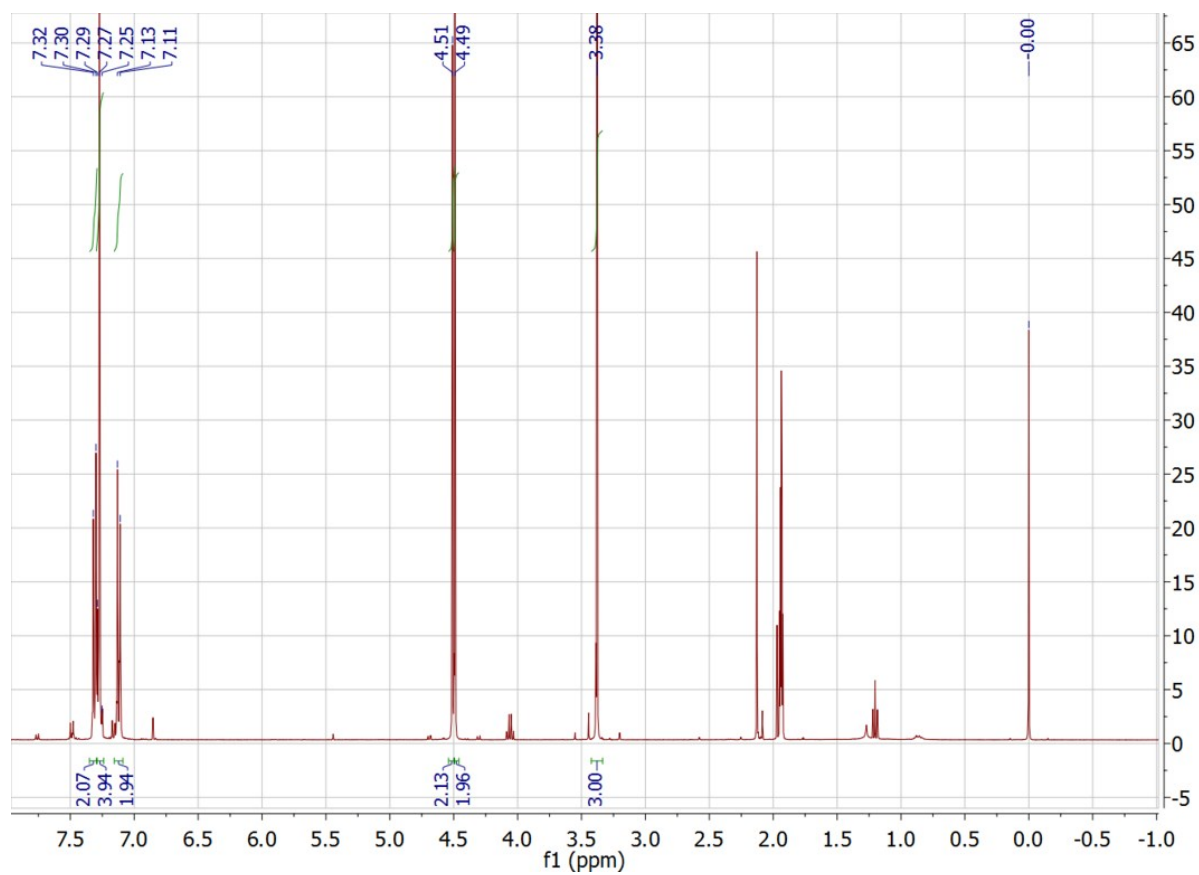
3.1 ^1H NMR spectra of 4'-methyl-N-methyl-N-(4-tolyl)benzamide in CDCl_3



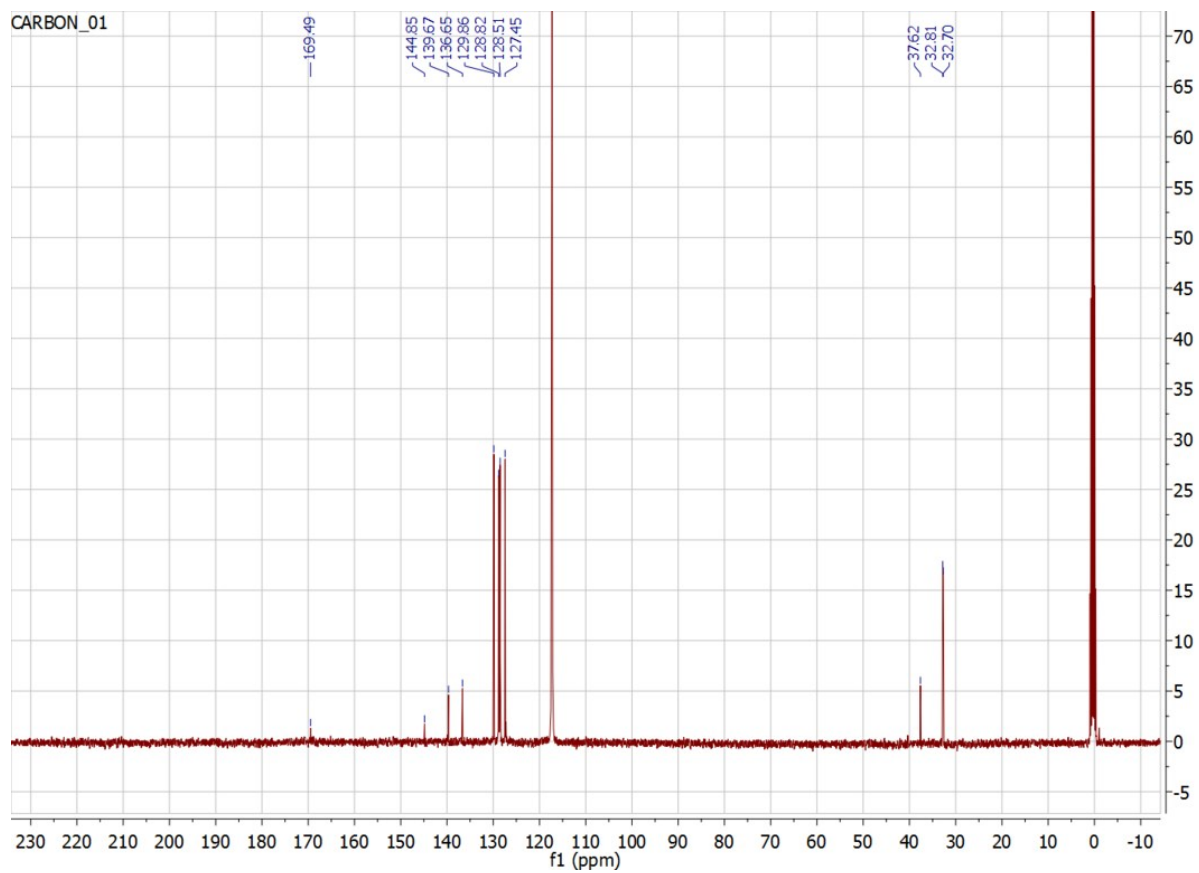
3.2 ^{13}C NMR spectra of 4'-methyl-N-methyl-N-(4-tolyl)benzamide in CDCl_3



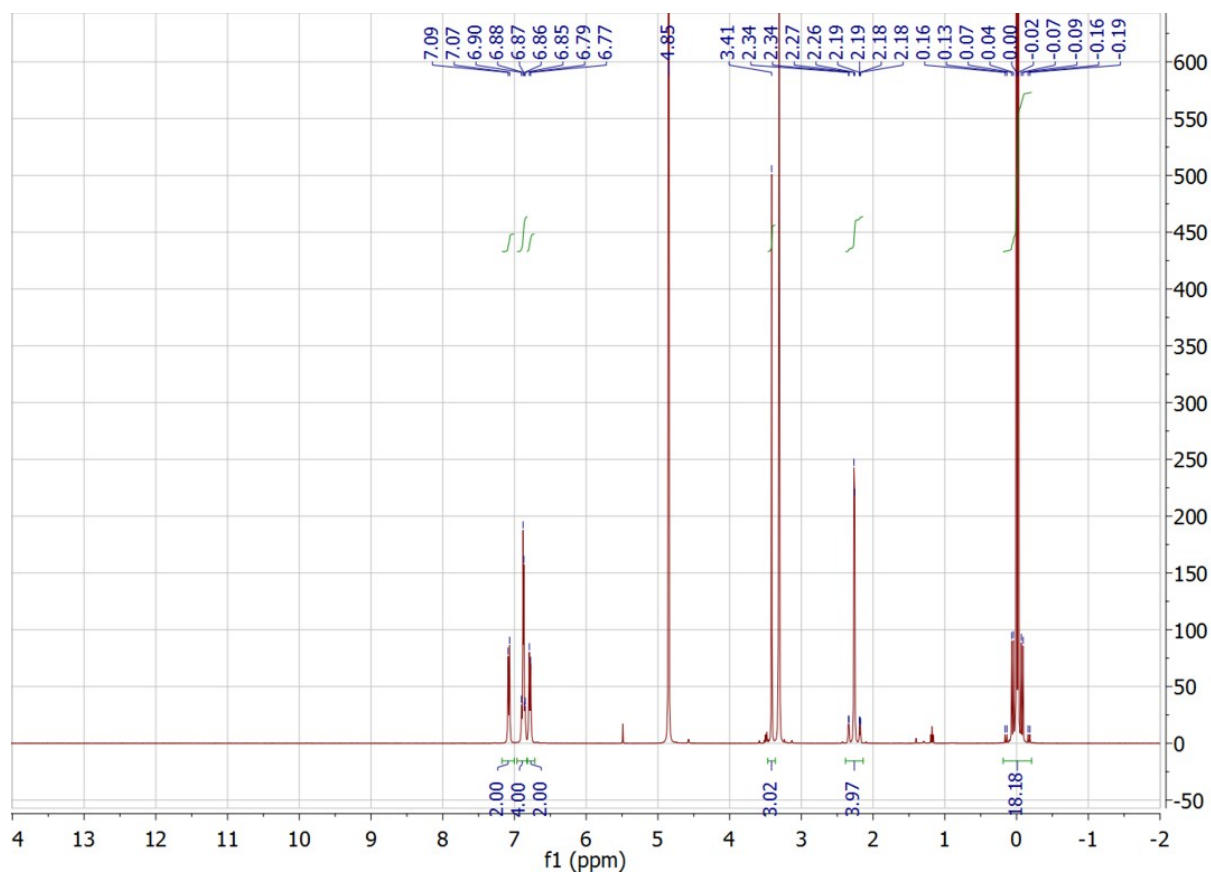
3.3 ^1H NMR spectra of 4'-bromomethyl-*N*-methyl-*N*-[4-(bromomethyl)phenyl]benzamide in CD_3CN



3.4 ^{13}C NMR spectra of 4'-bromomethyl-*N*-methyl-*N*-[4-(bromomethyl)phenyl]benzamide in CD_3CN

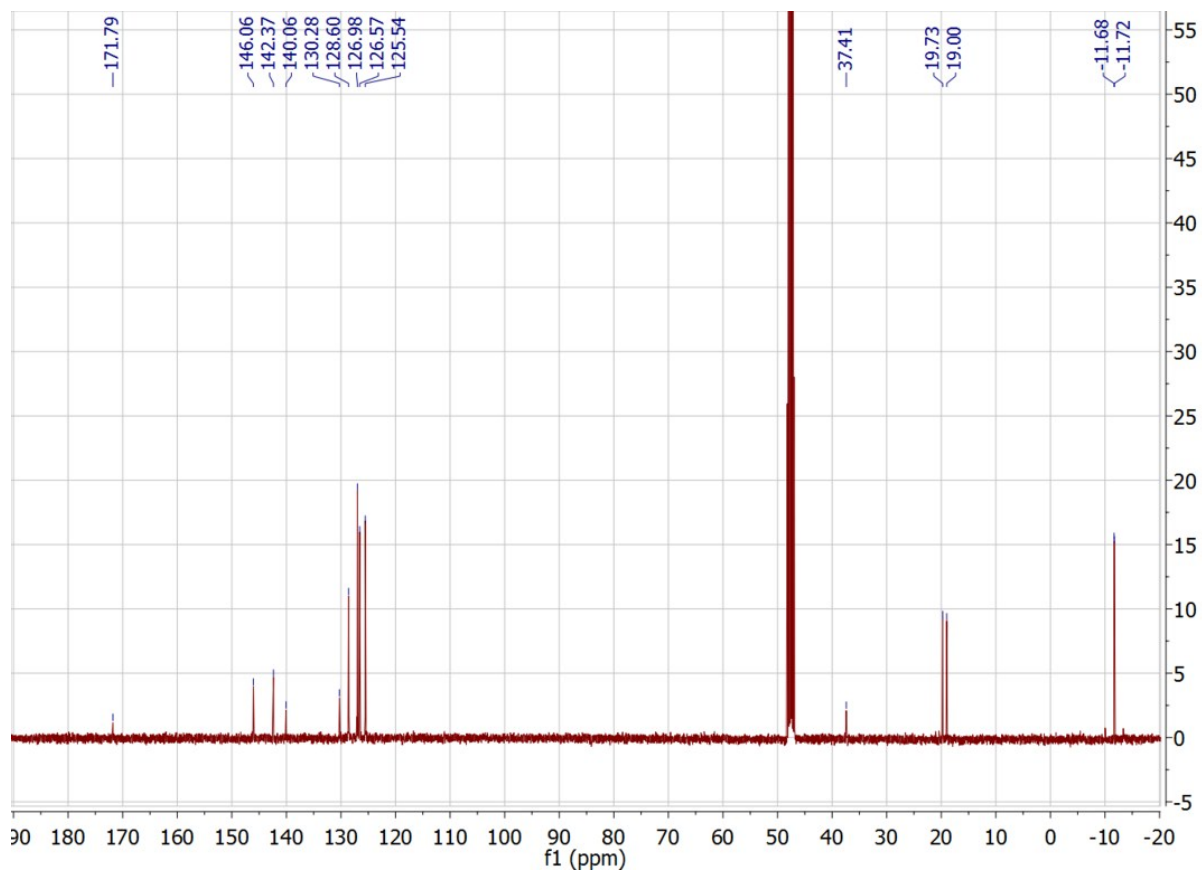


3.5 ^1H NMR spectra of 4'-(trimethylstannyl)methyl-*N*-methyl-*N*-[4((trimethylstannyl)methylphenyl)]benzamide in CD_3OD

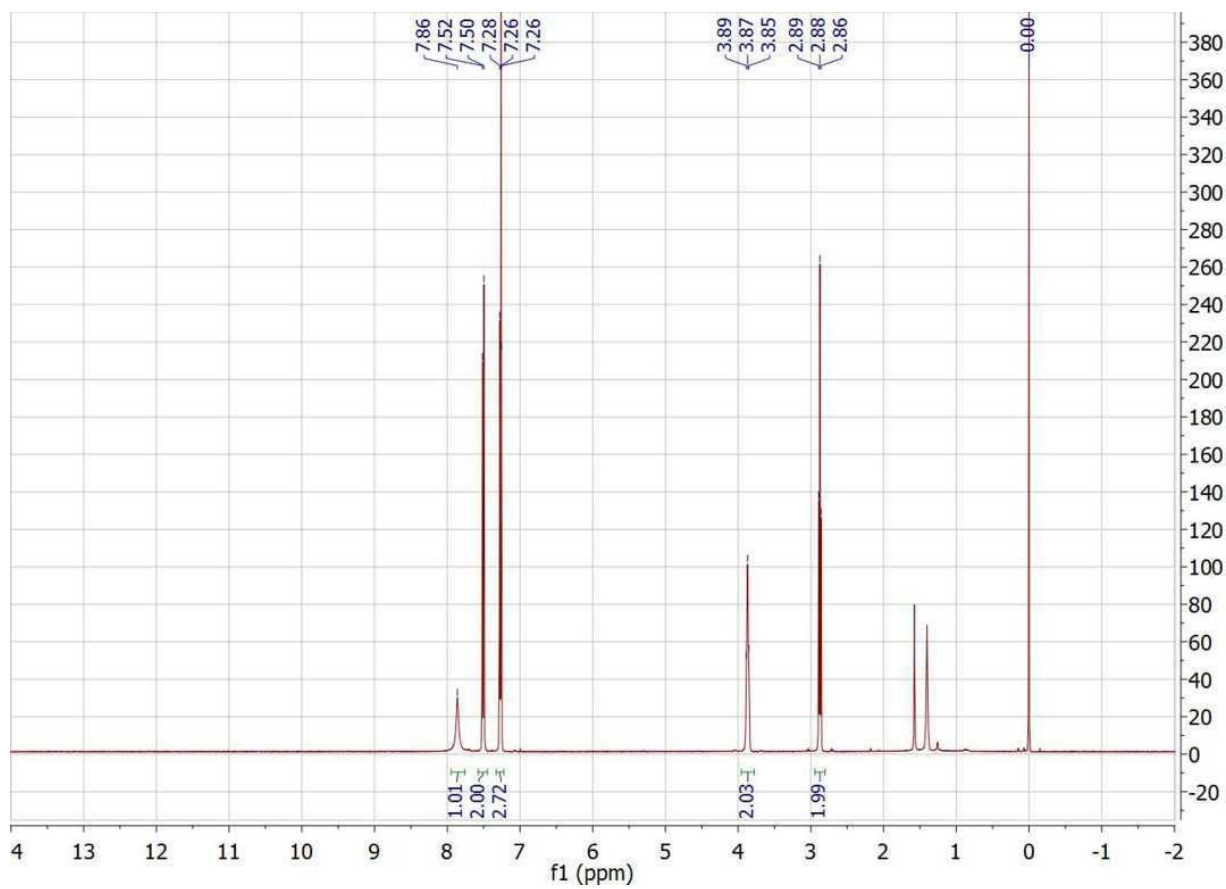


Residual solvent peaks (δ , ppm): CHD_2OD (3.31), H_2O (4.85), CHDCl_2 (5.49)

3.6 ^{13}C NMR spectra of 4'-(trimethylstannyl)methyl-*N*-methyl-*N*-[4((trimethylstannyl)methylphenyl)]benzamide in CD_3OD

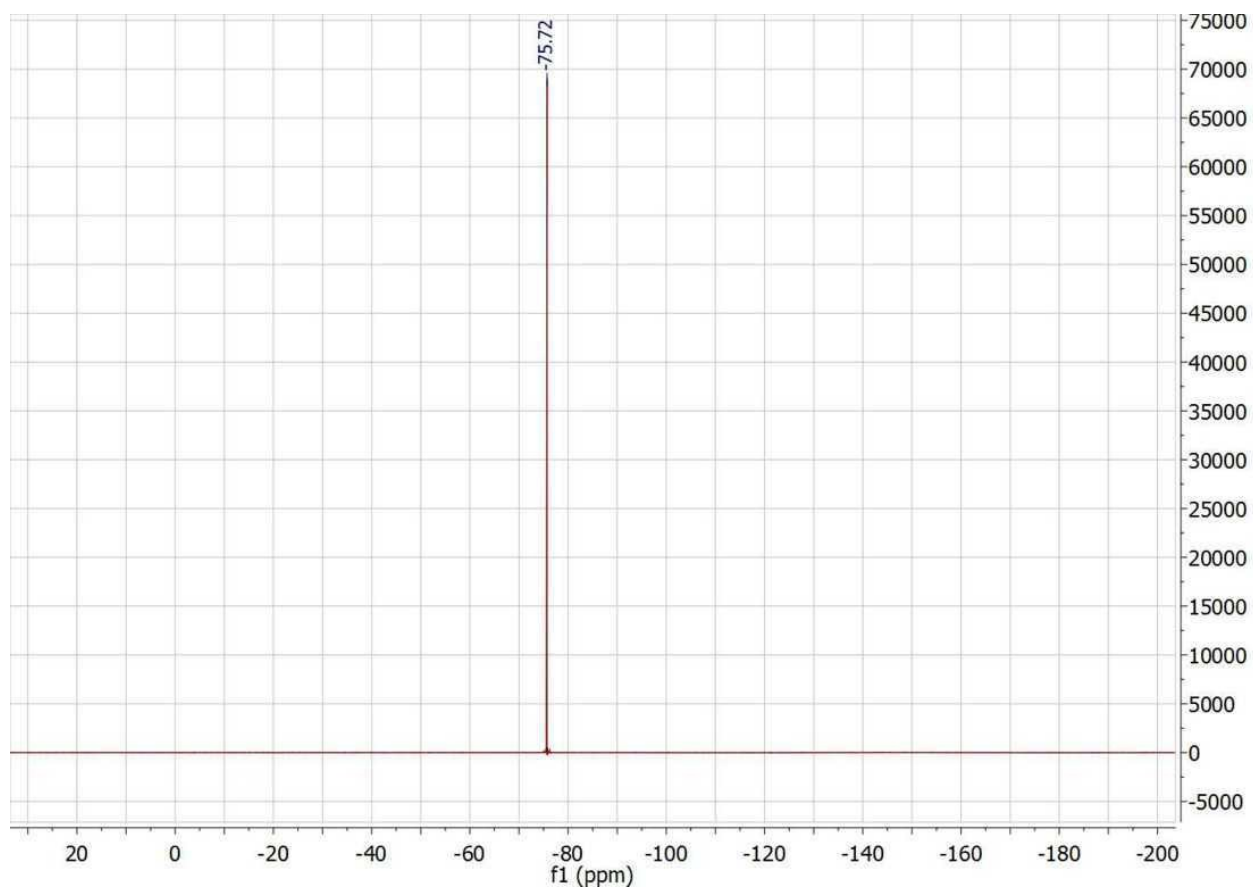


3.7 ^1H NMR spectra of 2[-4-(2',2',2'-trifluoroacetamido)phenyl]ethan-1-ol in CDCl_3

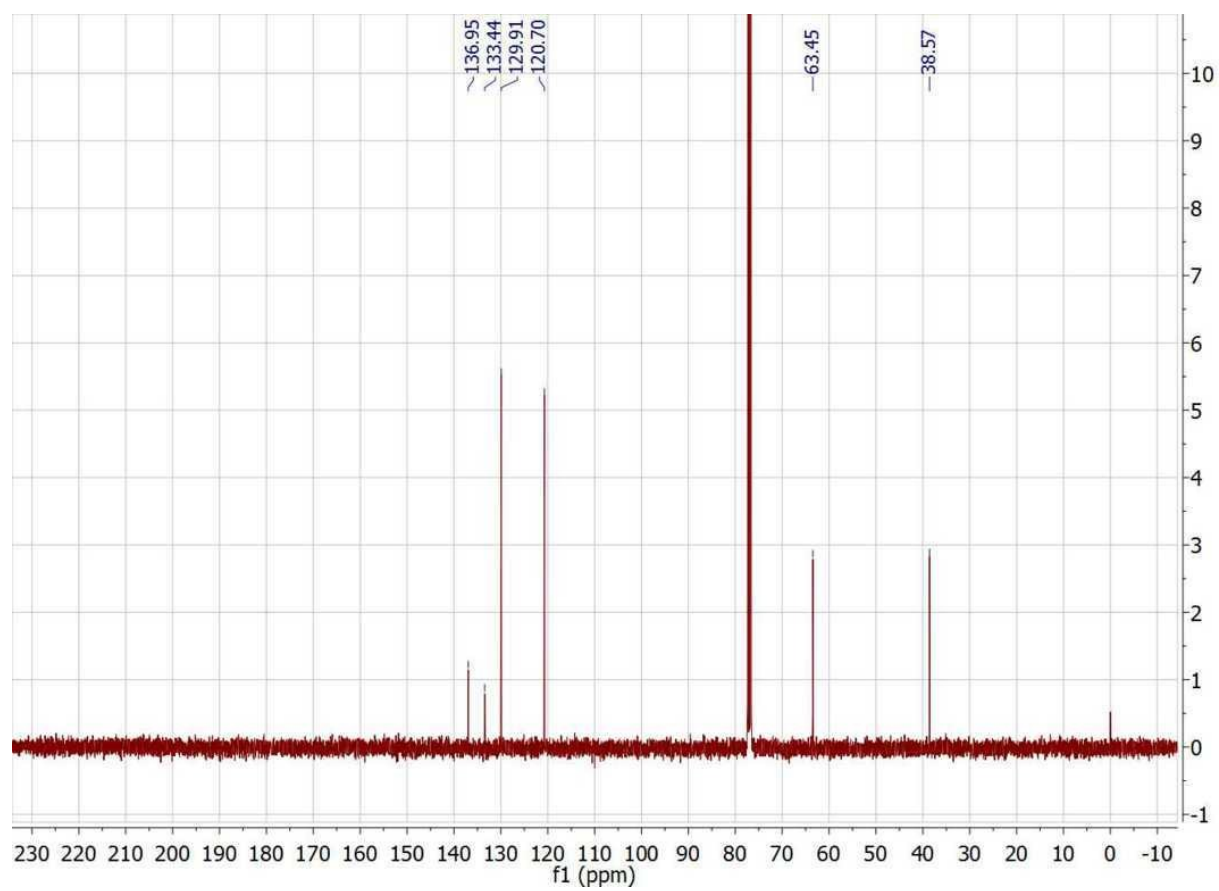


Residual solvent peaks (δ , ppm): CHCl_3 (7.26), H_2O (1.51)

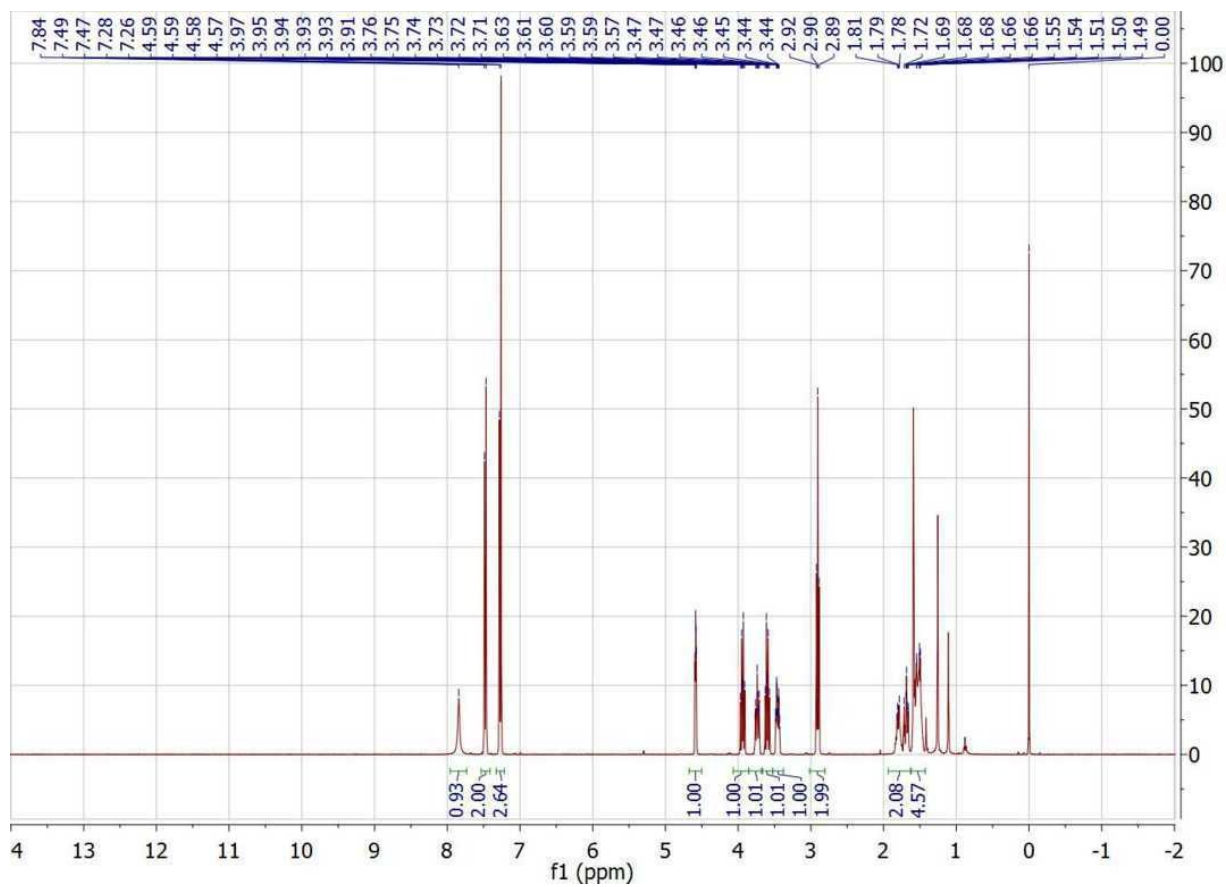
3.8 ^{19}F NMR spectra of 2[-4-(2',2',2'-trifluoroacetamido)phenyl]ethan-1-ol in CDCl_3



3.9 ^{13}C NMR spectra of 2[-4-(2',2'',2''-trifluoroacetamido)phenyl]ethan-1-ol in CDCl_3

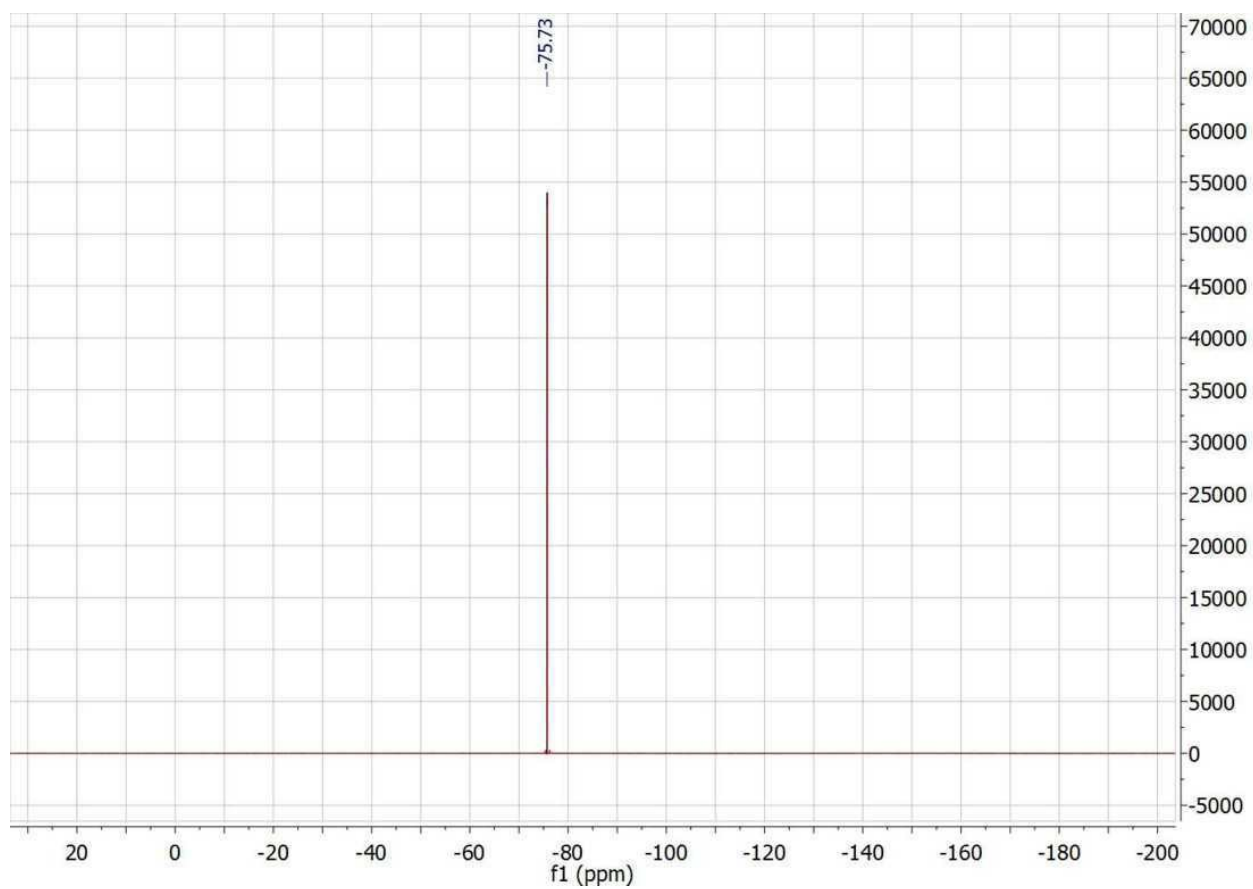


3.10 ¹H NMR spectra of 2,2,2-trifluoro-(4-(2-((tetrahydro-2H-pyran-2-yl)oxy)ethyl)phenyl)acetamide in CDCl₃

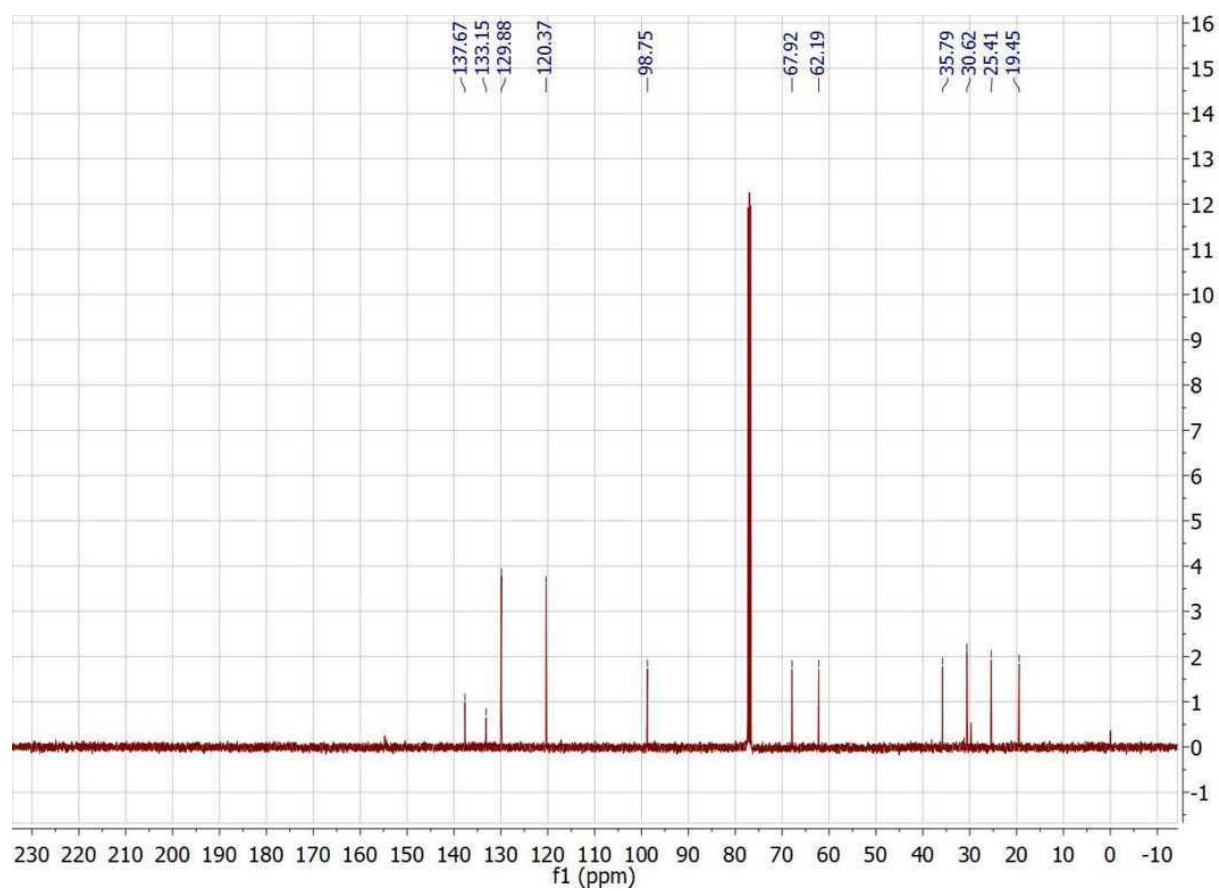


Residual solvent peaks (δ , ppm): CHCl₃ (7.26), H₂O (1.51)

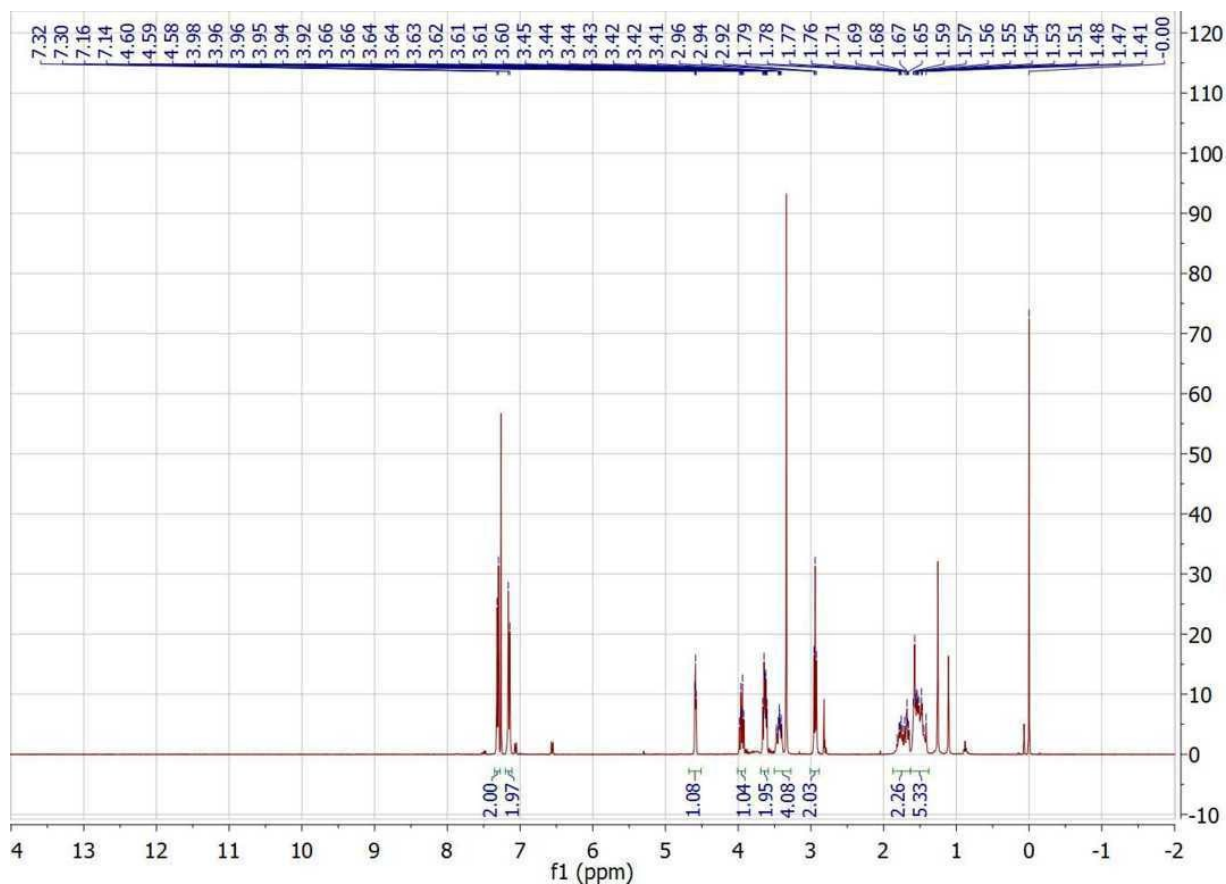
3.11 ^{19}F NMR spectra of 2,2,2-trifluoro-4-(2-((tetrahydro-2*H*-pyran-2-yl)oxy)ethyl)phenyl acetamide in CDCl_3



3.12 ^{13}C NMR spectra of 2,2,2-trifluoro-(4-(2-((tetrahydro-2*H*-pyran-2-yl)oxy)ethyl)phenyl)acetamide in CDCl_3

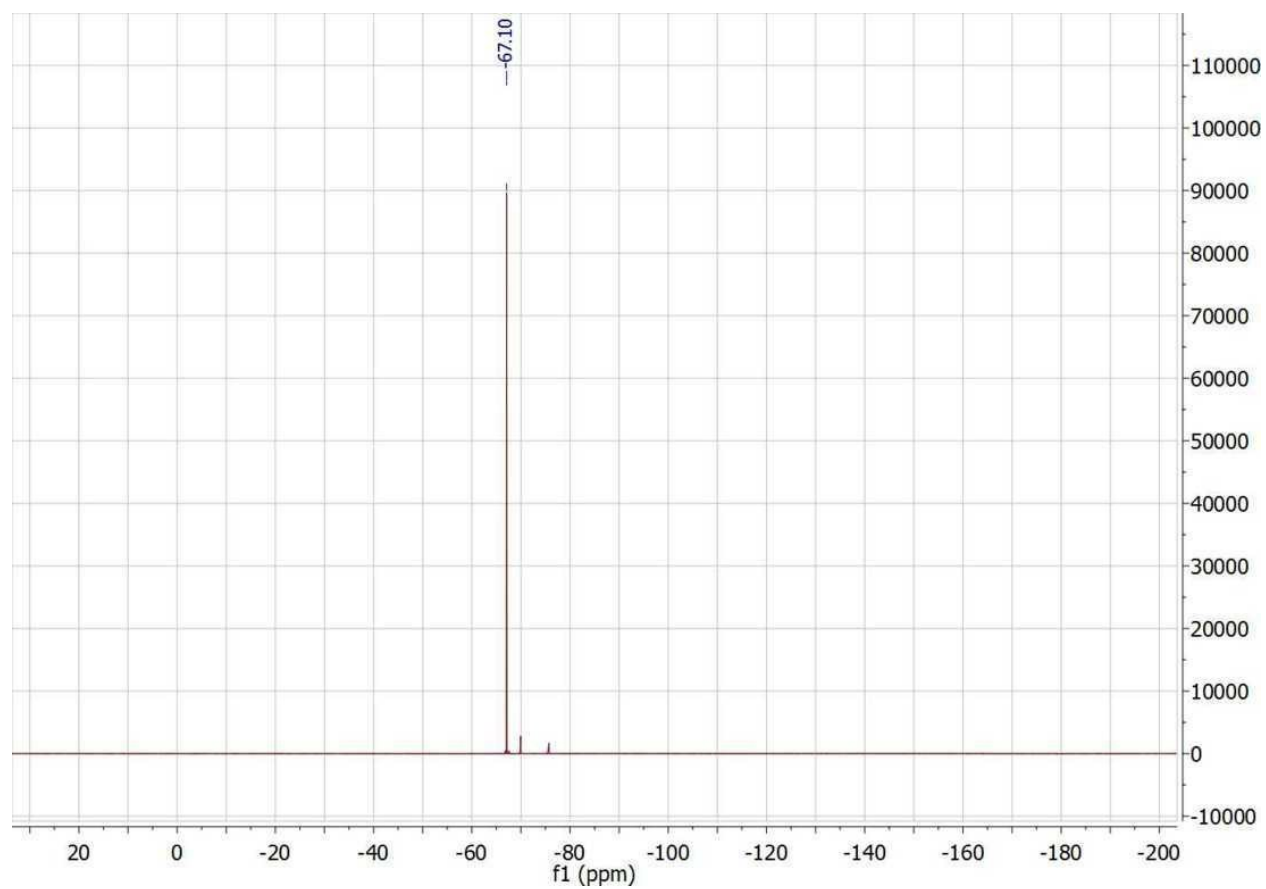


3.13 ^1H NMR spectra of 2,2,2-trifluoro-*N*-methyl-(4-(2-((tetrahydro-2*H*-pyran-2-yl)oxy)ethyl)-phenylacetamide in CDCl_3

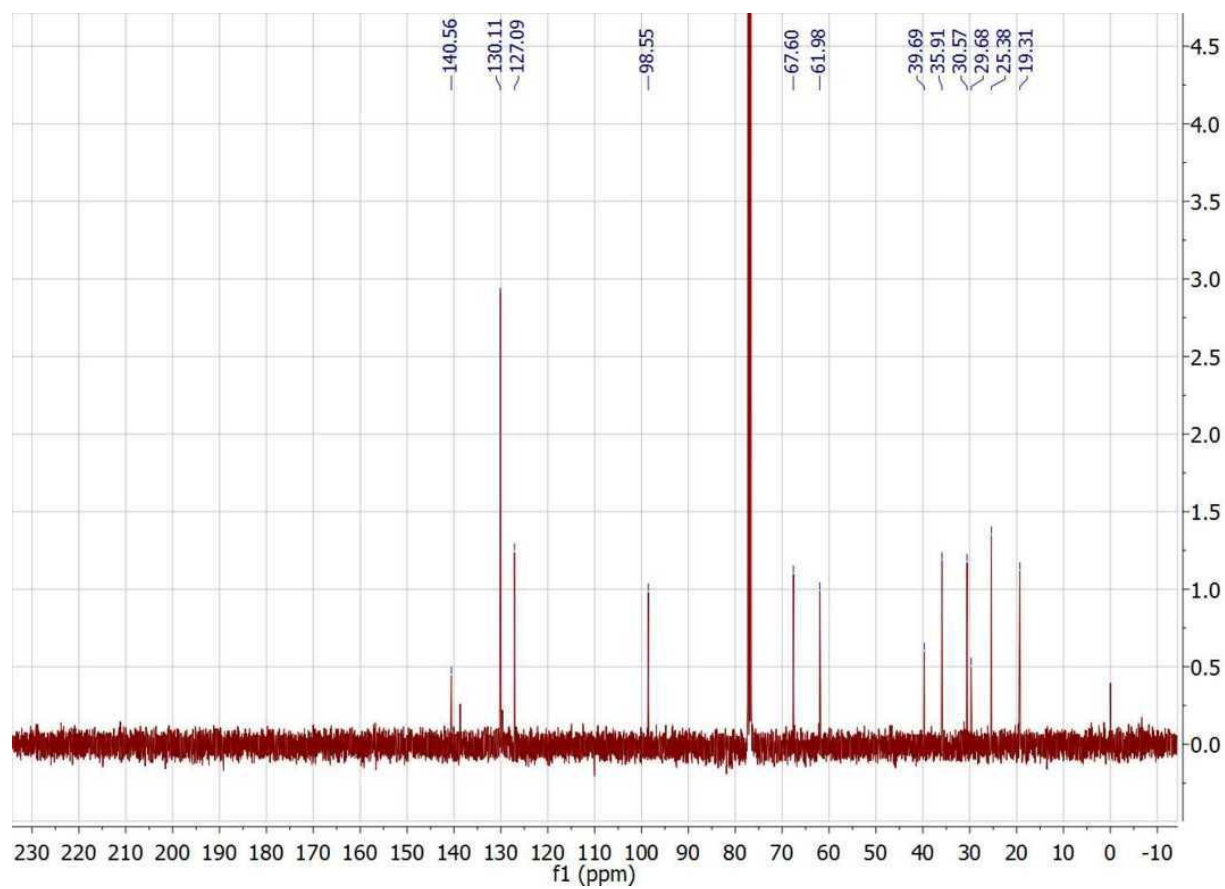


Residual solvent peaks (δ , ppm): CHCl_3 (7.26), H_2O (1.51)

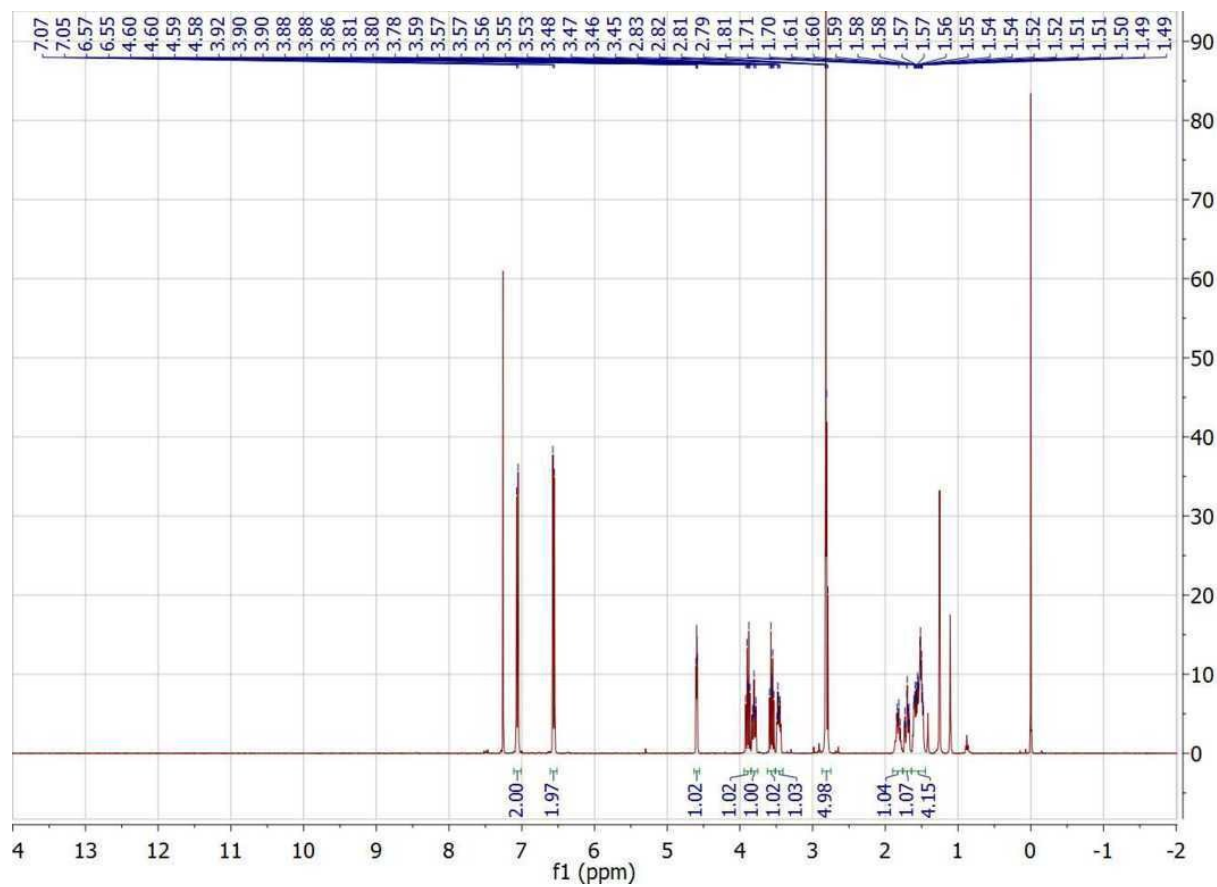
3.14 ^{19}F NMR spectra of 2,2,2-trifluoro-*N*-methyl-(4-(2-((tetrahydro-2*H*-pyran-2-yl)oxy)ethyl)-phenylacetamide in CDCl_3



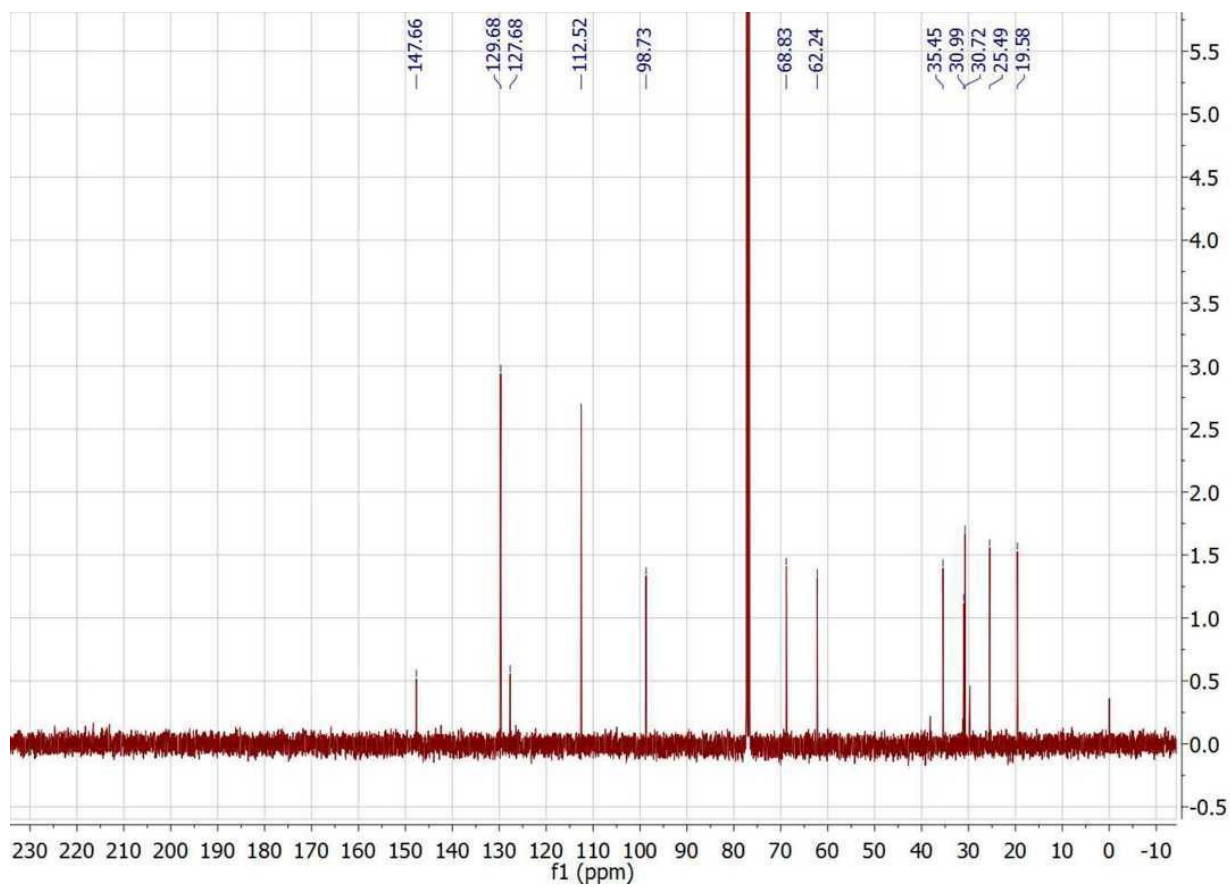
3.15 ^{13}C NMR spectra of 2,2,2-trifluoro-*N*-methyl-(4-(2-((tetrahydro-2*H*-pyran-2-yl)oxy)ethyl)-phenylacetamide in CDCl_3



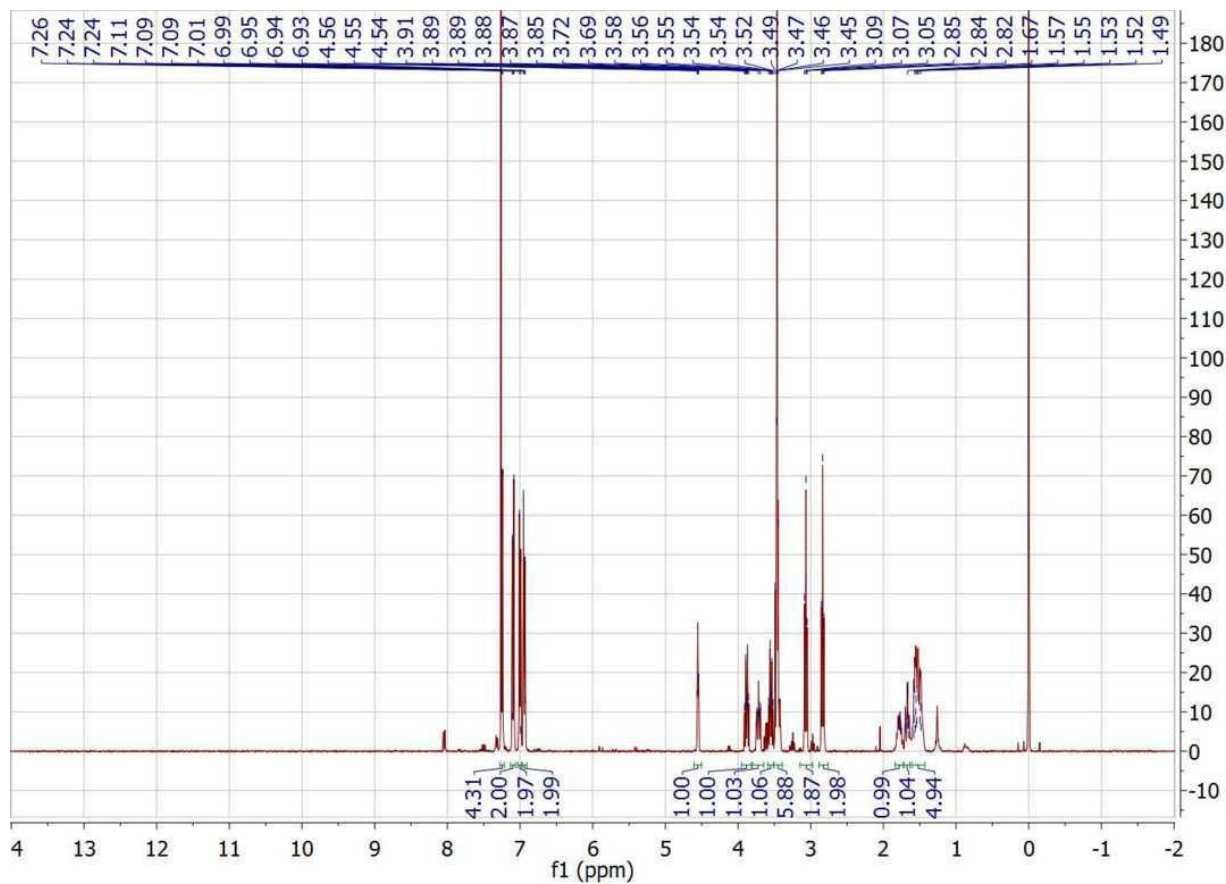
3.16 ^1H NMR spectra of *N*-methyl-4-(2-((tetrahydro-2*H*-pyran-2-yl)oxy)ethyl)aniline in CDCl_3



3.17 ^{13}C NMR spectra of *N*-methyl-(4-(2-((tetrahydro-2*H*-pyran-2-yl)oxy)ethyl)aniline in CDCl_3

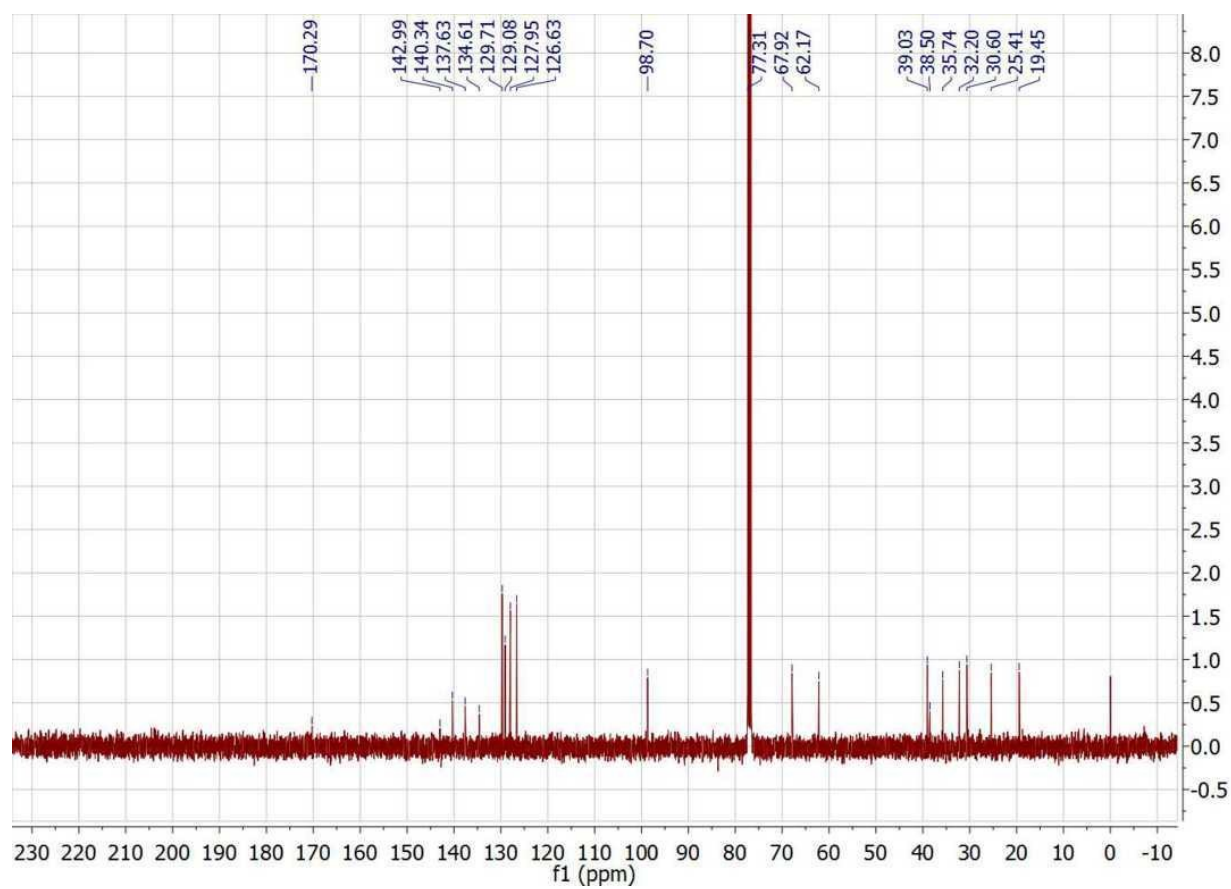


3.18 ^1H NMR spectra of 4-(2-bromoethyl)-*N*-methyl-*N*-(4-(2-((tetrahydro-2*H*-pyran-2-yl)oxy)-ethyl)phenyl)benzamide in CDCl_3

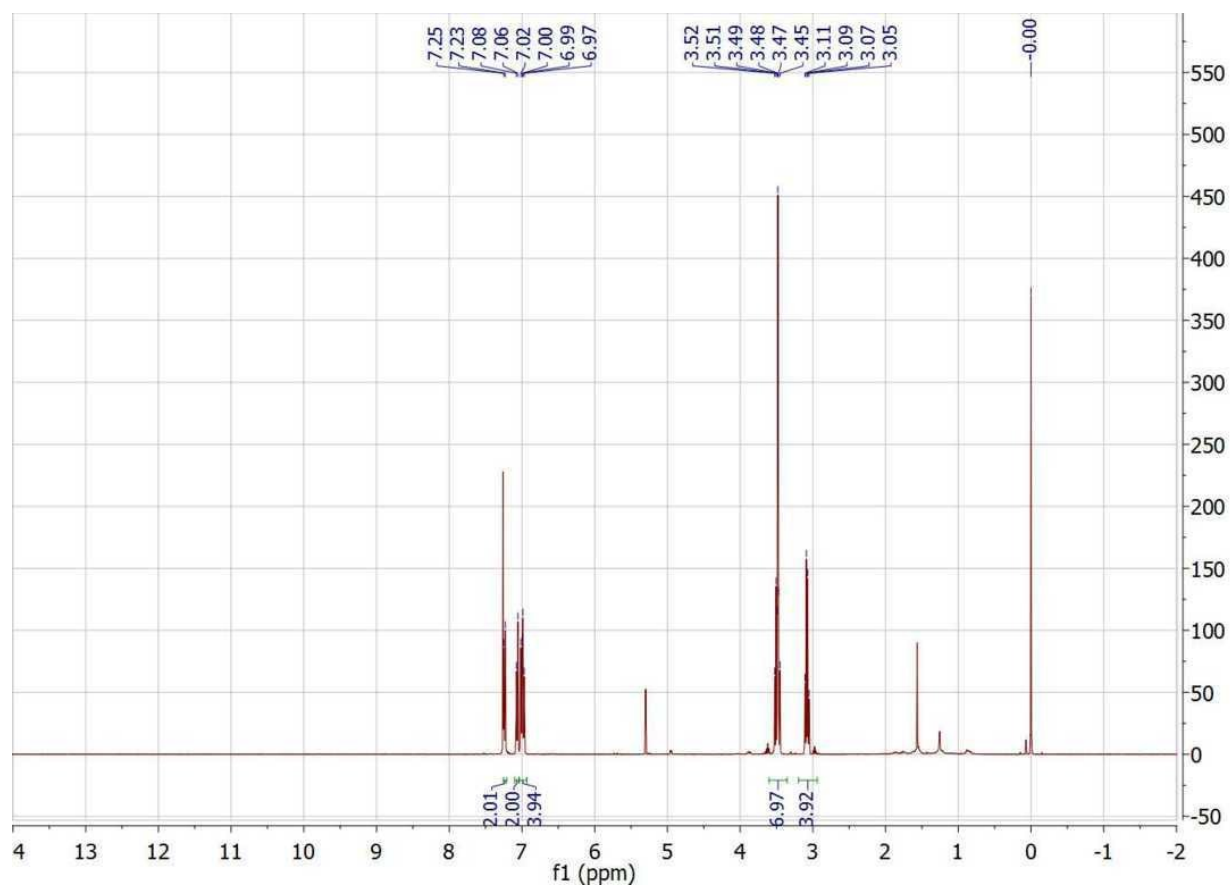


Residual solvent peaks (δ , ppm): CHCl_3 (7.26), H_2O (1.51)

3.19 ^{13}C NMR spectra of 4-(2-bromoethyl)-*N*-methyl-*N*-(4-(2-((tetrahydro-2*H*-pyran-2-yl)oxy)-ethyl)phenyl)benzamide in CDCl_3

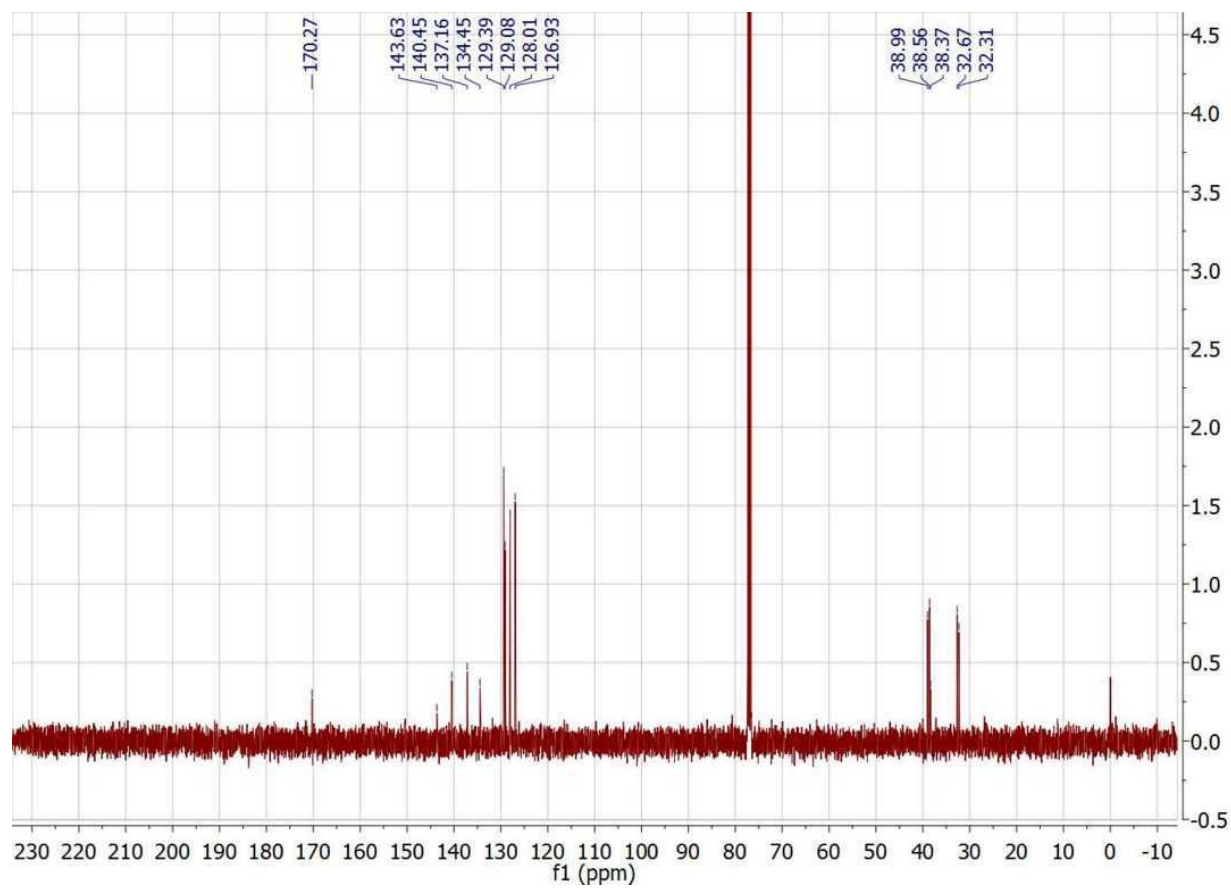


3.20 ^1H NMR spectra of 4-(2-bromoethyl)-*N*-methyl-*N*-(4-(2-bromoethyl)phenyl)benzamide in CDCl_3

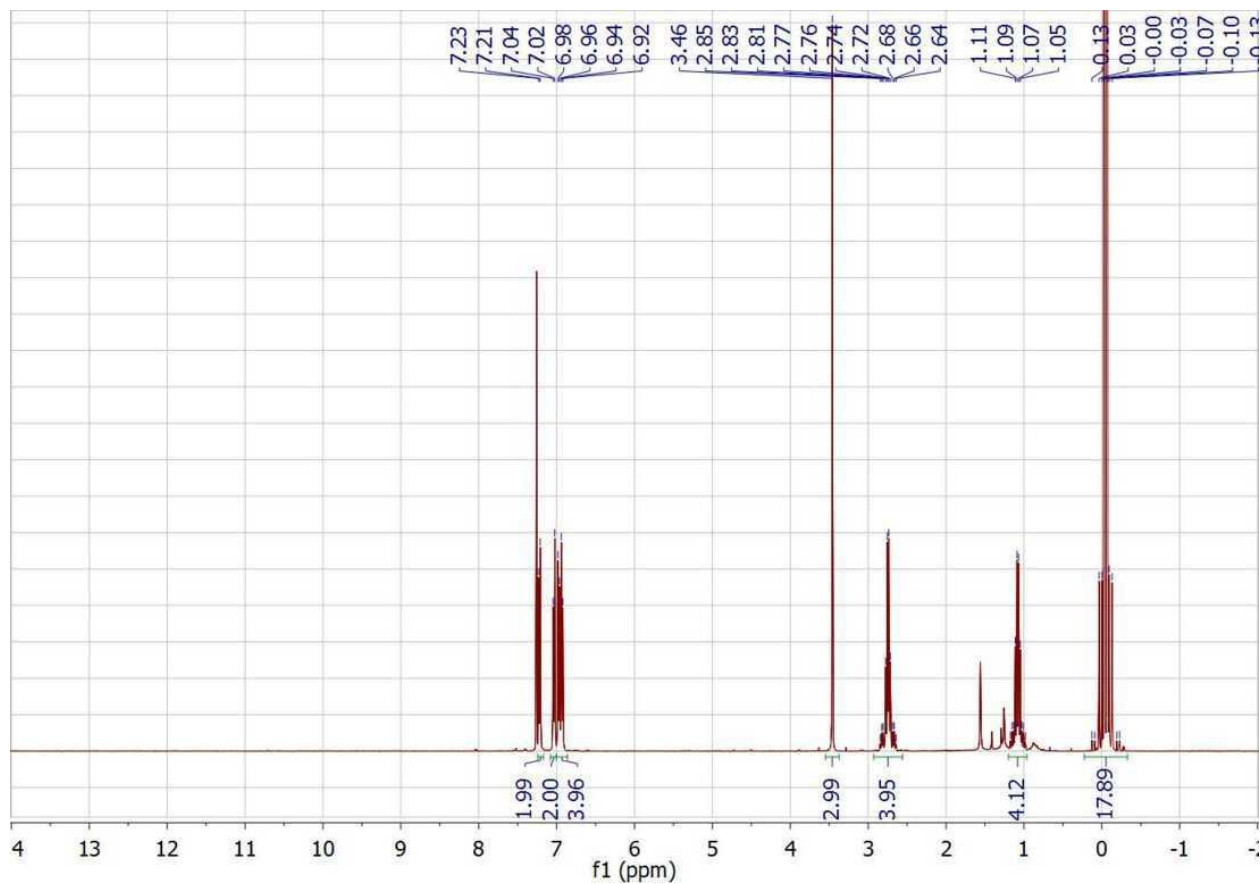


Residual solvent peaks (δ , ppm): CHCl_3 (7.26), H_2O (1.51)

3.21 ^{13}C NMR spectra of 4-(2-bromoethyl)-*N*-methyl-*N*-(4-(2-bromoethyl)phenyl)benzamide in CDCl_3

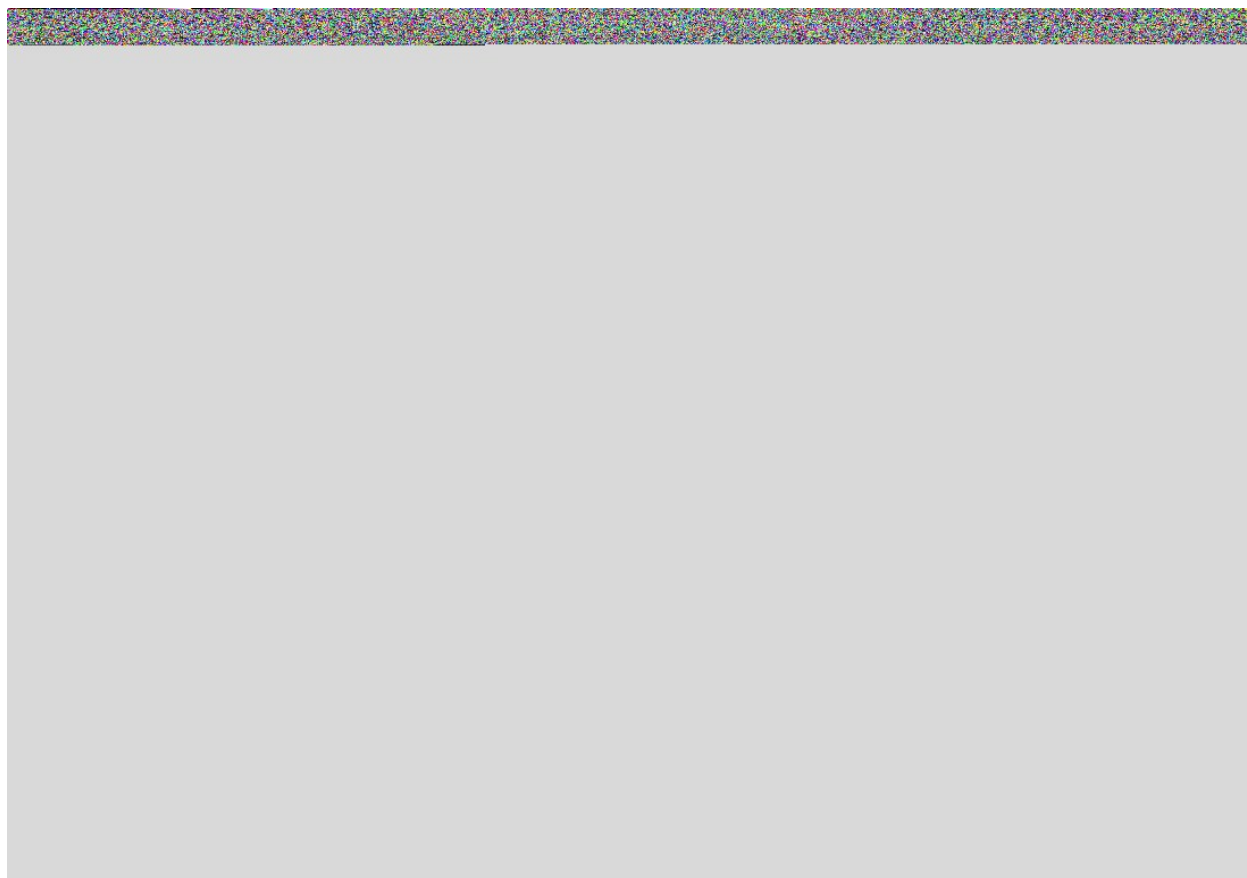


3.22 ^1H NMR spectra of 4-(trimethylstannyl)ethyl-*N*-methyl-*N*-(4((trimethylstannyl)ethyl)-phenyl)benzamide



Residual solvent peaks (δ , ppm): CHCl_3 (7.26), H_2O (1.51)

**3.23 ^{13}C NMR spectra of 4-(trimethylstannyl)ethyl-*N*-methyl-*N*-(4
((trimethylstannyl)ethyl)-phenyl)benzamide**



4. References

1. Koenigsmann, C.; Ding, W.; Koepf, M.; Batra, A.; Venkataraman, L.; Negre, C. F. A.; Brudvig, G. W.; Crabtree, R. H.; Batista, V. S.; Schmittenmaer, C. A. Structure-function relationships in single molecule rectification by N-phenylbenzamide derivatives. *New J Chem* **2016**, *In press* (DOI: 10.1039/C6NJ00870D).
2. Cuveas, J. C.; Elke, S. Nonequilibrium Green's functions formalism. In *Molecular Electronics*, World Scientific Printers: Singapore, 2010; Vol. 1, pp 179-203.
3. Ding, W.; Negre, C. F. A.; Vogt, L.; Batista, V. S. Single Molecule Rectification Induced by the Asymmetry of a Single Frontier Orbital. *Journal of Chemical Theory and Computation* **2014**, *10* (8), 3393-3400.
4. Ding, W.; Koepf, M.; Koenigsmann, C.; Batra, A.; Venkataraman, L.; Negre, C. F. A.; Brudvig, G. W.; Crabtree, R. H.; Schmittenmaer, C. A.; Batista, V. S. Computational Design of Intrinsic Molecular Rectifiers Based on Asymmetric Functionalization of N-Phenylbenzamide. *Journal of Chemical Theory and Computation* **2015**, *11* (12), 5888-5896.